TÜBİTAK

Turkish Journal of Earth Sciences

http://journals.tubitak.gov.tr/earth/

Research Article

Turkish J Earth Sci
(2023) 32: 577-600
© TÜBİTAK
doi:10.55730/1300-0985.1863

Textural and genetic investigations of gold mineralization in fault-controlled quartz-carbonate veins in Bayburt-Zarani area (Eastern Pontides-NE Turkey)

Necati TÜYSÜZ, Gülten YAYLALI-ABANUZ*, Oğuzhan GÜMRÜK, Bahrican AR
Department of Geological Engineering, Karadeniz Technical University, Trabzon, Turkey

Received: 02.12.2022 • **Accepted/Published Online:** 25.04.2023 • **Final Version:** 28.07.2023

Abstract: The Eastern Pontides Orogenic Belt (EPOB), geographically corresponding to the northeastern part of Turkey hosts several different types of mineralizations that are closely related to Late Mesozoic-Early Cenozoic arc magmatism. Of these, Zarani gold mineralization, which is located in the southern part of the EPOB occurs as quartz-carbonate veins/veinlets within the Pulur metamorphic massif of Paleozoic age.

Mineral textures indicate low-temperature vein-type mineralization. Gold mainly occurs in quartz and pyrite. The presence of calcite, dolomite, and sericite in the mineralization indicates near neutral pH conditions of ore-forming fluid. Geochemical analyses of chlorites in the quartz-carbonate veins reveal a temperature of ore formation at 140–297 °C, which is compatible with those obtained from fluid inclusions in the mineralized quartz (i.e. 132–226 °C). The average salinity value obtained from fluid inclusions is 4.32% NaCl equiv. O and H isotope values range from –6.03‰ to +1.47‰ and from –60‰ to –119‰, respectively, indicating a mixture of magmatic and meteoric fluids. Mixing is also evidenced by the X_{Fe} analytical data of hydrothermal chlorites associated with ore-forming gangue minerals. Gold precipitation in Zarani mineralization is caused by boiling. The occurrence of mineralization within quartz-carbonate vein/veinlets in metamorphic host rocks, the mineral paragenesis with near-neutral pH conditions of the ore-forming low salinity fluids and the H–O isotopic data imply that the Zarani gold mineralization is an orogenic type epithermal mineralization that may be related to deeply buried Early Cenozoic felsic intrusions, produced by subduction-induced processes in the southern part of the EPOB.

Key words: Eastern Pontides Orogenic Belt, epithermal gold, vein-type, stable isotope, fluid inclusion

1. Introduction

The Eastern Pontides Orogenic Belt (EPOB) is one of the well-preserved fossil magmatic arcs in the Alpine-Himalayan orogenic system. As with many magmatic arcs, the EPOB also hosts several types of ore deposits, which have been the subject of numerous studies (e.g., Güven, 1993; Tüysüz et al., 1995; Akçay et al., 1998; Tüysüz, 2000; Lermi, 2003; Demir et al., 2008; Yaylalı-Abanuz and Tüysüz, 2010, 2011; Akaryalı and Tüysüz, 2013; Eyuboglu et al., 2014; Akaryalı, 2016; Delibaş et al., 2016; Revan, 2020). The most important ones of these deposits, from north to south, are Kuroko-like volcanogenic massive sulfide (VMS) type Cu-Pb-Zn deposits associated with the Late Cretaceous felsic extrusive rock series (e.g., Murgul, Tunca, Çayeli, Kutlular, Harköy, Lahanos), porphyry Cu±Mo and skarn deposits associated with the Early (?) and Late Cretaceous felsic intrusions (e.g., İspir-Ulutaş, Yomra-Özdil, Maçka-Güzelyayla, Merzifon-Bakırçay) and epithermal gold deposits associated with Early Cenozoic magmatism (e.g., Artvin-Cerattepe, Gümüşhane-Mastra, Gümüşhane-Kaletaş, Gümüşhane-Arzular, Ordu-Akoluk, Ordu-Sayaca, Fatsa-Altıntepe). Considering the type, origin, and regional distribution of ore deposits, the EPOB is divided into three major metallogenic belts from north to south: volcanogenic massive sulfide, porphyry Cu-Mo and skarn, and epithermal gold. Most of these deposits are small-scale and exploited and abandoned, except Mastra (producing > 25 t of gold) and Altıntepe epithermal gold, and Çayeli and Murgul VMS deposits.

There is a limited number of studies on the origin of gold mineralizations that occur mainly in the southern part of the EPOB. Geological, petrographic and geochemical data indicate that they are mainly intermediate-sulfidation epithermal in the origin (Aslan, 2011; Akaryalı and Tüysüz, 2013; Akaryalı, 2016; Akaryalı and Akbulut, 2016), except Kaletaş mineralization, which is a sedimentary-hosted Carlin-type gold deposit (Tüysüz and Çubukçu, 1999). They are generally hosted by Eocene volcano-sedimentary rocks consisting mainly of andesitic-basaltic volcanic and associated pyroclastic and are mainly controlled by NW-SE and NE-SW-trending structures. Eyuboglu et al., (2011, 2013, and 2017) classified the Eocene felsic

* Correspondence: gultenyaylali@yahoo.com

intrusions exposed in the southern part of the EPOB into two main categories as adakitic and nonadakitic, based on their geochemical characteristics, and suggested that the Lutetian nonadakitic granitoids, which are well exposed along the Gümüşhane-Bayburt-İspir welt, were probably responsible for the economic epithermal gold mineralizations in the EPOB.

The Zarani gold mineralization is located immediately south of the Gümüşhane-Bayburt-İspir welt defined as an epithermal gold belt by Eyuboglu et al. (2011 and 2017) in the southern part of the EPOB and is hosted by medium- to high-grade lithologies of Pulur metamorphic massif. To date, there has been only one study on this mineralization, which was exploration-oriented (Güner and Yazıcı, 2012). In this study, we present new geological, petrographic, tectonic, whole-rock major and trace element, oxygen and hydrogen isotope, fluid inclusion, and mineral chemistry data from the Zarani gold mineralization and discuss its genesis in the light of new and published data.

2. Geological background

The EPOB stretches over a length of 600 km and a width of 200 km that extends parallel to the southeastern coast of the Black Sea (Figure 1). The Mesozoic-Cenozoic geodynamic evolution of EPOB has been a subject of some controversy over the last forty years. The most widely accepted idea is that the EPOB was shaped by the northward subduction of Tethyan (either Paleotethys or Northern Branch of Neotethys) oceanic lithosphere in the Late Mesozoic and subsequent collision of Eastern Taurides with Eastern Pontides in the Early Cenozoic (e.g., Adamia et al., 1977; Şengör and Yılmaz, 1981; Okay and Şahintürk, 1997; Arslan and Aslan, 2006; Karslı et al., 2007; Aydin et al., 2020; Kaygusuz et al., 2020). Conversely, some researchers suggested that the EPOB was formed above a south-dipping subduction zone from Paleozoic to Early Cenozoic (Dewey et al., 1973; Bektaş, 1987; Bektaş et al., 1999; Eyuboglu et al., 2011, 2017, 2018, 2019, 2021; Maden and Elmas, 2022).

The EPOB can be divided into three subzones: the northern, southern, and axial zones, based on different lithological units, facies changes, and tectonic characteristics (Bektaş et al., 1995; Eyuboglu et al., 2006). Each zone is separated by NE, NW, and E-W trending regional faults which control the emplacement of most of the felsic intrusions and associated mineralizations. The Northern Zone is mainly represented by the Late Mesozoic and Early Cenozoic volcanic and plutonic rocks. The Carboniferous to Triassic metamorphic

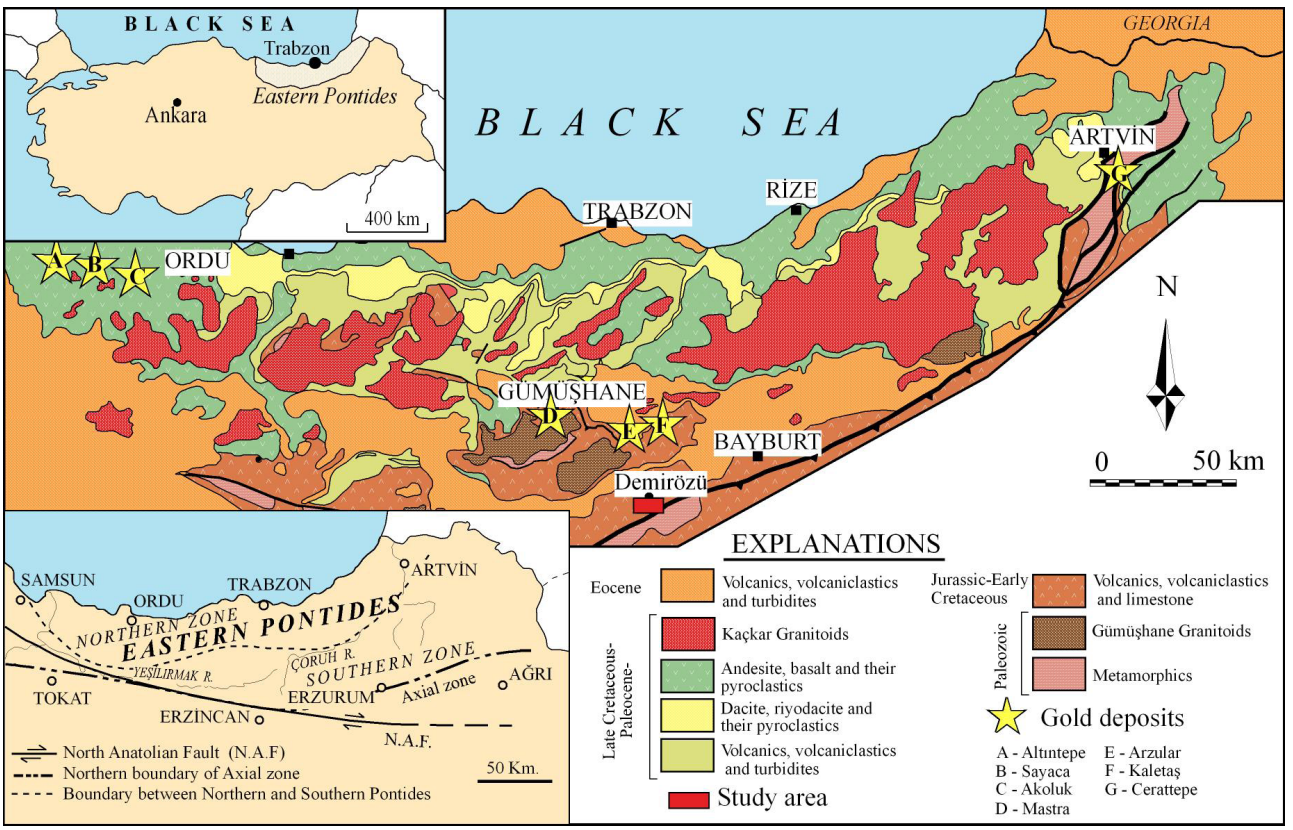

Figure 1. Geological map showing the distribution of the main lithological units and gold deposits in the EPOB (modified after Güven, 1993).

lithologies including Pulur, Ağvanis, and Tokat massifs, the Late Carboniferous Gümüşhane and Köse granitoids and Alaskan-type ultramafic-mafic complexes, Early to Middle Jurassic volcano-sedimentary rocks, Late Jurassic to Early Cretaceous carbonate rocks, Late Cretaceous clastic rock-dominated sequences and high-K volcanic and plutonic rocks, Late Paleocene to Early Eocene adakitic intrusions, Lutetian basaltic-andesitic volcanic and felsic plutonic rocks are the main lithological units exposed in the Southern Zone of the EPOB. Serpentinized ultramafics, an ophiolitic oliststromal melange unit, and Mio-Pliocene volcanic and sedimentary rock assemblages are widespread in the Axial Zone that extends between the Eastern Pontides and Eastern Taurides blocks (Figure 1).

The Zarani gold deposition is located 7 km south of Demirözü town, which is 30 km WSW of Bayburt city in the southern part of the EPOB. In this region, the oldest rock unit is the Paleozoic Pulur metamorphic massif, comprising two different tectonometamorphic units (Topuz et al., 2004). The high-grade Cenci Unit includes mainly gneiss, amphibolite, and migmatite whereas the low-grade Doğankavak Unit consists predominantly of metabasite, phyllite, schist, and metachert. Pulur metamorphic massif was cut by Late Carboniferous nonmetamorphic Alaskan-type mafic-ultramafic intrusions (Eyuboglu et al., 2010) and unconformably overlain by Early to Middle Jurassic volcano-sedimentary rocks (Hamurkesen Formation) which grades upward into Late Jurassic to Early Cretaceous carbonate sequence (Berdiga Formation) and continues with Middle to Early Late Cretaceous olistostromal ophiolitic melange unit. The whole sequence is cut by Ypresian adakitic porphyritic and plutonic intrusions (Topuz et al., 2005; Eyuboglu et al., 2011) and is unconformably overlain by a Lutetian clastic rock-dominated sequence (Sırataşlar Formation).

3. Ore geology and structural setting

NE- and NW-trending fractures, resulting from N-S compression are the main tectonic feature of the EPOB. The distribution of the sedimentary basins, plutons, and mineralizations in the region is controlled by these fracture systems (e.g., Bektaş et al., 1995, 1999; Eyuboglu et al., 2006).

The gold-bearing quartz-carbonate veins occur within an N40–60 °E trending and 50–70°NW dipping fracture zone developed in the Pulur Metamorphic Massif (Figure 2). The veins have a thickness of about 10 m over a strike length ranging from 50 m to 300 m. Their thickness diminishes at depths. The metamorphic lithologies include silicified zones, which are enriched primarily with gold, pyrite, and Cu-minerals. Alteration zones comprising mainly of silicification, sericitization and carbonatization with about 5–50 m width and 50–100 m lenght occur over a fracture zone of 3.5 km. Faults in the fracture zone are extending in two different directions. One of them trending in N60°W along the Dağtarla River in the north is not mineralized. On the other hand, the fault zone (Zarani-main fault zone) extending 40–60° NE direction is mineralized. The 60° NW-trending fault is younger than those with mineralization at the northern edge. This fault zone consists of several faults with strike lengths ranging from a few ten to hundreds of m. The mineralizations are recognized along the main fault zone as intermittent vein/veinlets with varying thicknesses. Fracture plane measurements taken from mineralized areas on the major fault and kinematic analysis based on field and drilling data indicate that the main fault in the study area was defined as an N57°E trending right-lateral strike-slip fault with transtensional character and it is accompanied by 35°NE and 75°NE trending splay-faults and riedel shears (Figures 3a and b). Although anti-riedel fractures and faults are not recognized in this resolution, the fault around the north of Sakızlı site in the north of area is thought to be anti-riedel type. It is believed that shear fault starts along the foliation planes within the calcschists-micaschists and then gains a transtensional character depending on pull-apart basin development in the EPOB (Bektaş et al., 1995). In areas where dips of riedel and splay faults are increased (up to 80°–85°) mineralizations are thickened (A–A^1 section in Figure 4). Since this is a common feature of dip-slip normal faults, it is suggested that the strike-slip fault wherever it gained oblique (transtensional) character acted as normal faults and hence created open spaces. Opening and shearing caused a grid-like fracture pattern forming stockworks that are filled with quartz-carbonate veinlets (Figure 5). These veinlets create quartz-carbonate-cemented breccias forming rhombic-shaped wall rocks fragments between the fault and veins. These observations indicate that host rock around the fault zone is broken and fragmented by the shear zone and then opened cyclically as a result of transtensional movements and finally filled with quartz and carbonate material with accompanied ore minerals.

3.1. Textural and microstructural features

Several studies have shown that silica and carbonate phases have various textures revealing the physical conditions related to mineralization in the hydrothermal deposits. These different textures are divided into three groups. These are primary growth textures that formed during the deposition, recrystallization textures, and replacement textures (Adams, 1920; Bodnar et al., 1985; Sander and Black, 1988; Saunders, 1990; Dong et al., 1995; Henley and Hughes, 2000; Camprubi and Albinson, 2007; Moncada et al., 2012; Yilmaz et al., 2016). The textures observed in the veins are mainly open-space, although some recrystallization textures are also noted.

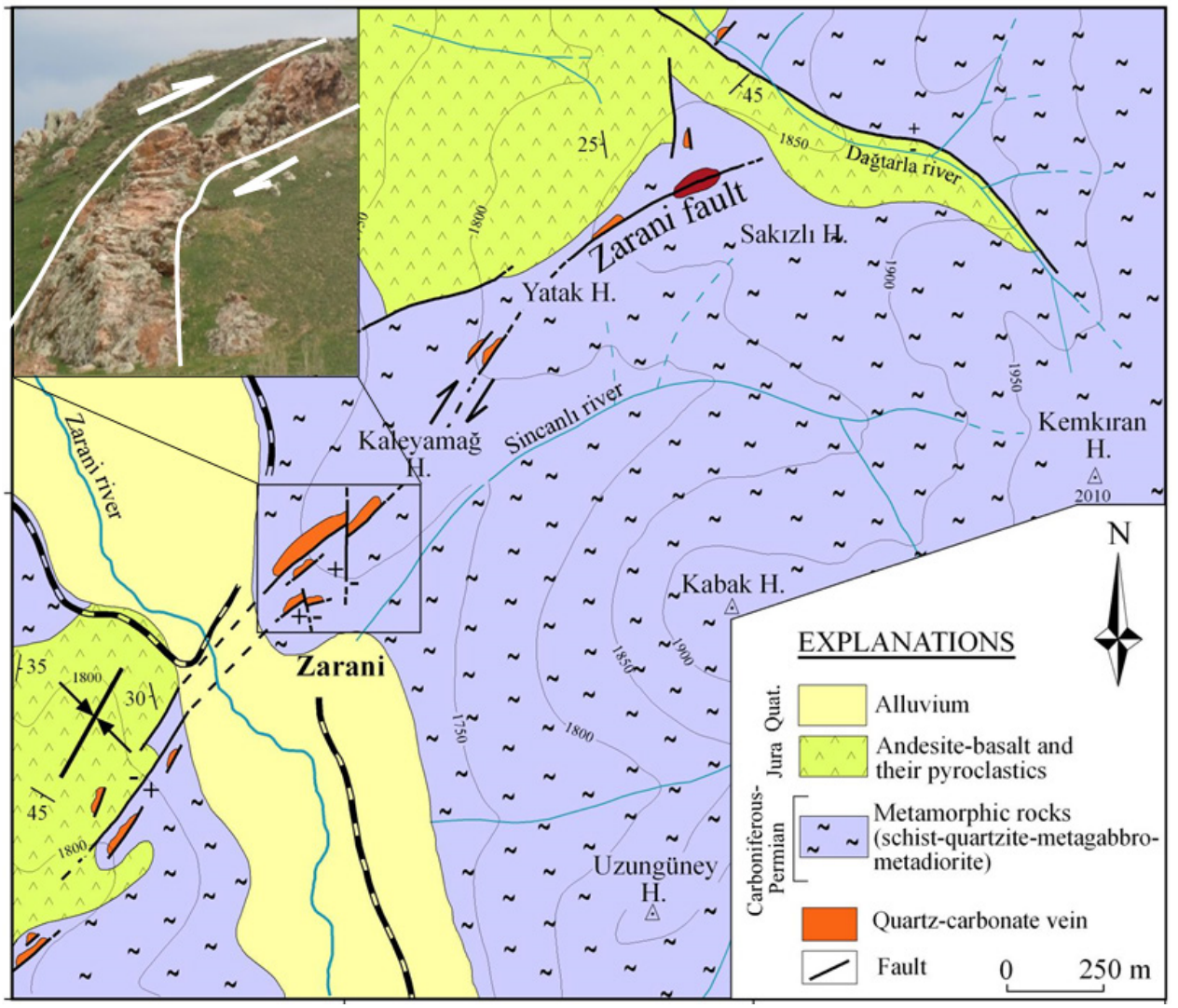

Figure 2. Geological map of Zarani (Bayburt-Demirözü) ore field (modified after Güner and Yazıcı, 2012).

The comb texture is characteristic of euhedral quartz crystals that grow from a nuclei surface in the empty zones to the space center. It can be either double or single-sided. Comb-texture quartz was recognized in a few samples, and it is the primary growth texture (Figures 6a and b). Quartz represented by this type of texture has micro-fractures that host secondary inclusions (Bodnar et al., 1985).

The void-filling texture is one of the most common textures recognized in epithermal systems. The voids could be either primary or dissolution voids that form as a result of faulting and fracturing of the rock. In the quartz-carbonate veins of the Zarani ore field void texture is quite common (Figures 6c and 6d).

The brecciation occurs by the fragmentation of hematitic and silicified veins due to shearing. The voids are widely filled by quartz and carbonate minerals (Figures 6e and 6f).

The mosaic texture that is one of the texture types observed in the quartz minerals of Zarani ore field is characterized by interlocking of grain boundaries of microcrystalline or crystalline quartz crystals (Dong et al., 1995) and this feature is recognized by only a microscopic study. This mosaic texture is formed by recrystallization of chalcedony or amorphous silica (Dong et al., 1995; Camprubi and Albinson, 2007).

The massive texture is also observed in quartz-carbonate veins. The "massive" term is used to refer to the homogeneous appearance of quartz minerals and the absence of banding and deformation (Dong et al., 1995).

The flamboyant texture was first described by Adams (1920) and Sander and Black (1988). Under a microscope,

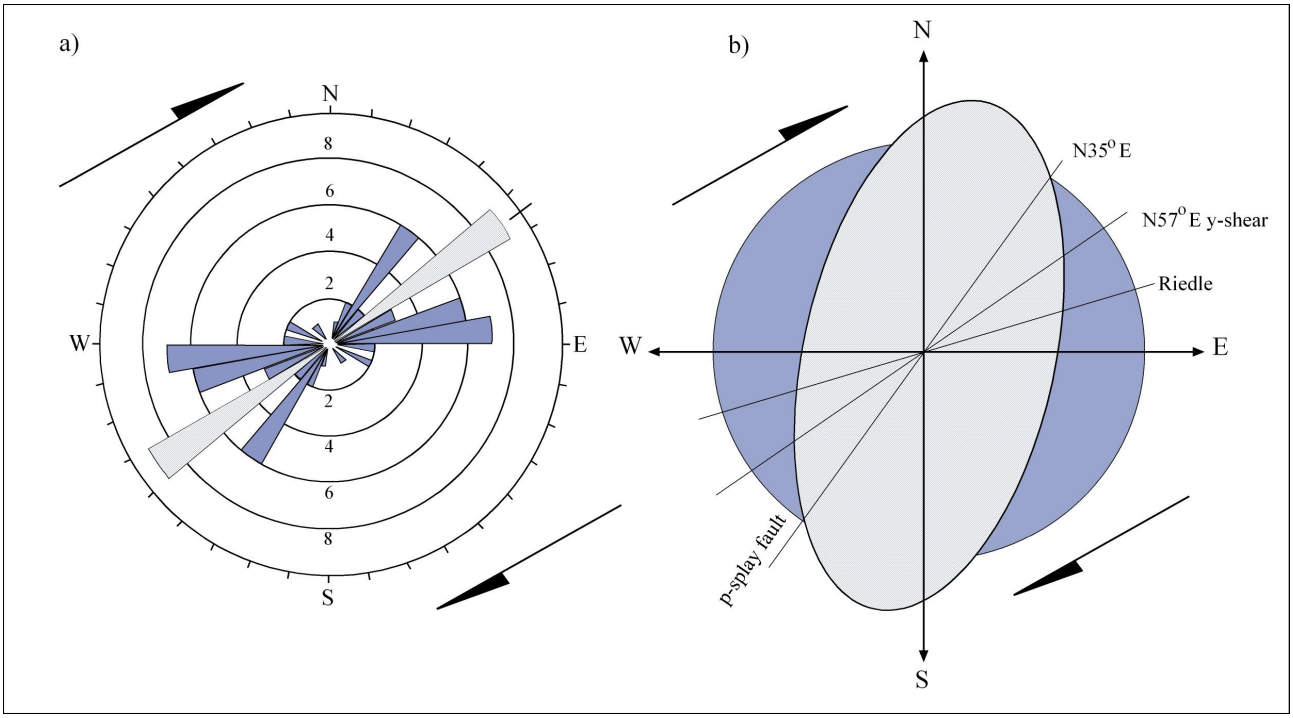

Figure 3. a) Rose plot of strike and dip amount values of the Zarani fault plane (main fault) together with associated structures. b) Strain ellipsoid indicating the development of a N57°E trending main fault accompanied by N35°E and N75°E trending splay faults and riedel shears formed by a dextral shear regime in the Zarani area.

euhedral quartz crystals show extinction from the rims to the center (Figure 7a), similar to the feathery texture. The term feathery originates from spine-like appearance of quartz crystals. For this texture, different names are used just like for flamboyant and plumose quartz textures (Dong et al., 1995; Moncada et al., 2012). It is thought that the recrystallization texture is made up of silica gel and consists of fibrous microcrystalline quartz, which is rounded along the outer rims (Dong et al., 1995). The silica gel is deposited during supersaturation that is triggered by faulting and boiling subsequent to rapid pressure and temperature decrease (Henley and Hughes, 2000). This type of silica comprises the transition phase in the silica deposition cycle and it is deposited following the amorphous silica phase but before the crystalline quartz phase (Camprubi and Albinson, 2007). Feathery and plumose textures are common within the studied samples (Figures 7b, 7c, 7d, 7e).

Zoned quartz texture is a primary growth texture and resembles comb texture (Figure 7f). In this texture, euhedral quartz crystals show growth zones that host primary inclusions reflecting the original deposition conditions (Moncada et al., 2012).

Microscopic determinations revealed that the size of quartz crystals ranged from very fine to very coarse. They grow along their long axis (Figures 7g and 7h). Mosaic, feathery, plumose, and colloform textures recognized in the studied samples are formed by quartz crystallization from silica or directly deposition from the supersaturated solution.

3.2. Ore petrography

The gold mineralization in the Zarani field mainly includes sulfide and oxide minerals that occur in veins/veinlets within the silicified zones. Among the sulphide minerals, pyrite is the most dominant phase associated with chalcopyrite, bornite, and tennantite in the hypogene stage. Malachite, hematite, limonite, and covellite occur in the supergene stage. Quartz, dolomite, calcite, sericite, and chlorite are the primary gangue minerals (Figure 8).

Pyrite occurs as euhedral to subhedral grains frequently showing a cataclastic texture and is replaced by other ore minerals such as chalcopyrite, rutile, and hematite (Figures 9a, 9b, 9c, 9d). Chalcopyrite as the second most common ore mineral occurs in subhedral to anhedral forms replacing and surrounding pyrites. Chalcopyrite is locally replaced by bornite and tennantite (Figures 9c and 9d). Bornite is a minor constituent of the mineralization and occurs as subhedral fine grains (Figure 9c) and is replaced by tennantite. Tennantite is also rarely observed as small anhedral grains and replaces both chalcopyrite and

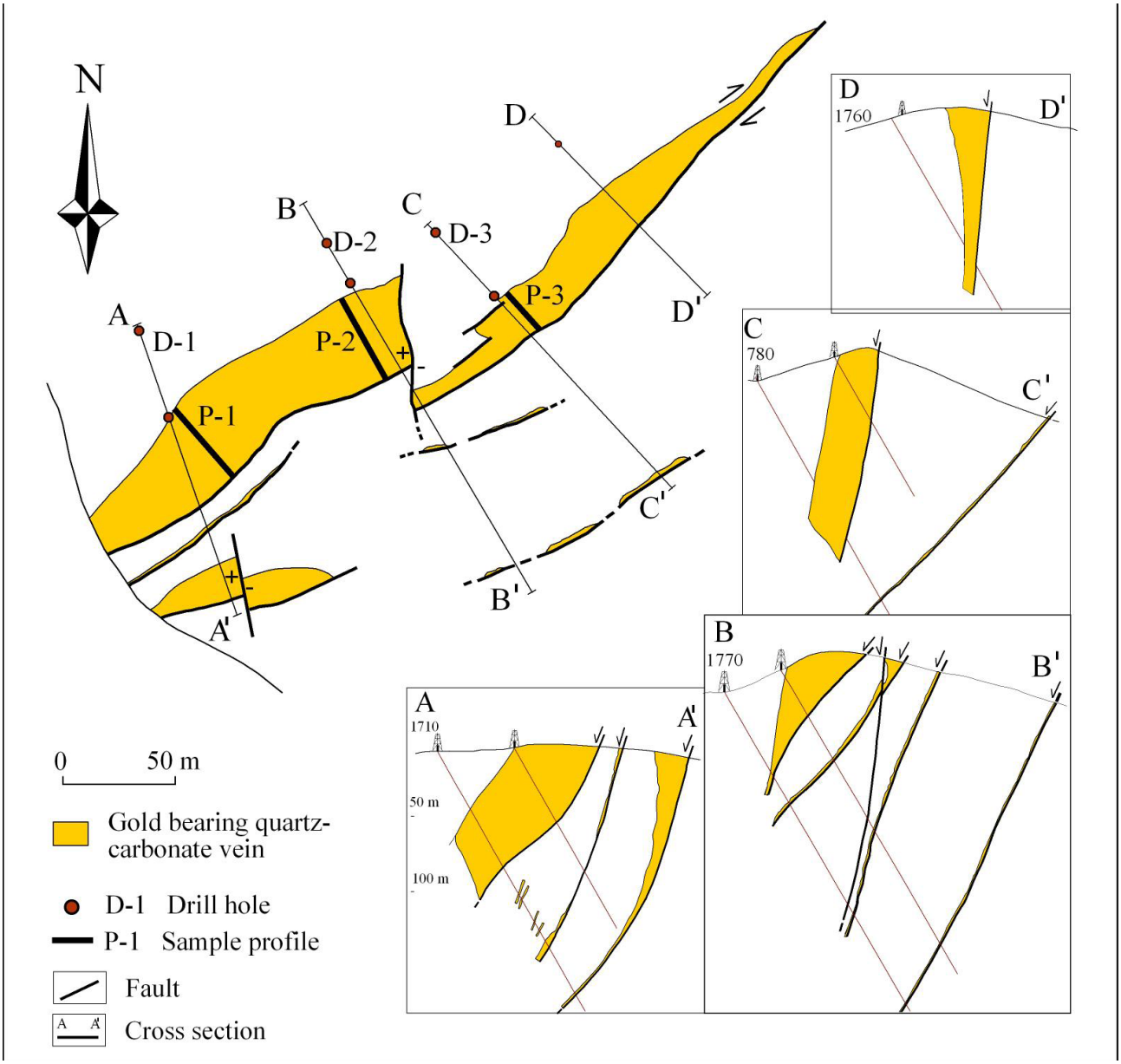

Figure 4. A planar and cross-section views of gold bearing quartz-carbonate veins showing the flaring upwards geometry with decreasing thickness towards the depth.

bornite (Figures 9c and 9d). Covellite occurs as anhedral grains replacing chalcopyrite (Figure 9e) and is recorded as the supergene phase product.

The gold in bright yellow color coexists with quartz in the gangue ranging from 5 to 20 μm in size (Figure 9f). In addition, it forms part of the pyrite crystal structure as determined by EPMA analyses. The analyses of pyrite minerals indicate significant amounts of gold content with an average of 0.760 (wt.%) Au reaching up to 0.176 (wt.%) Au (Table 1). Gold does not show any significant relationship with other ore-forming elements in pyrites. Samples collected for chemical analyses (Table 2) from D-1, D-2, and D-3 boreholes drilled in and from P-1, P-2, and P-3 profiles laid out on quartz-carbonate veins revealed gold concentrations varying from 0.50 to 9761 μg/kg with an average of 209.6 μg/kg.

Hematite is macroscopically pale red in color and occurs mostly as decomposed grains (Figure 10b). Limonite is yellow in color and occurs as an alteration product of pyrite.

3.3. Hydrothermal alteration

There is a limited alteration exposed in the surface of the study area. However, silicification, carbonatization,

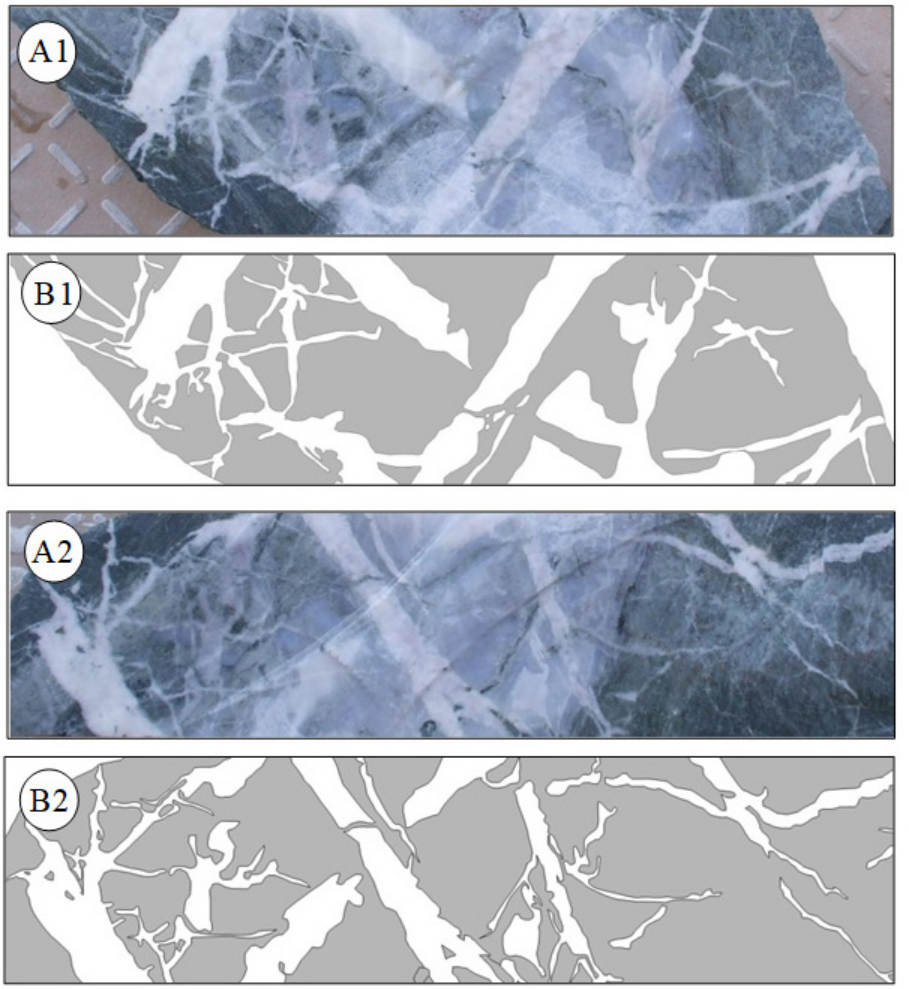

Figure 5. Core samples (a1, a2) showing brecciation supported by quartz-carbonate cement occurring in association with shearing and opening fractures. b1 and b2 are the sketches.

sericitization, and a minor amount of chloritization occur in quartz-carbonate veins along the fault zones. These alterations are controlled by a NE–SW trending fracture system. Propylitic alteration outside of the fracture system is represented by calcite and chlorite. Disseminated pyrite is common within the quartz-carbonate veins. Drilling data indicated the presence of an alteration zone with a width of 50–60 m (quartz vein + altered silicified zone), which is related to gold mineralization.

XRD analysis reveals the presence of abundant kaolinite and illite with minor smectite. Kaolinite and illite occur in the vicinity of quartz-carbonate veins and smectite is found in low quantity away from the fracture system.

3.4. Chlorite chemistry

Hydrothermal chlorite grains occur as small clusters (Figure 10a) and veinlets associated with quartz, calcite, dolomite, sericite, pyrite and chalcopyrite indicating that chlorite was at least partly contemporaneous with these phases, whereas that of metamorphic origin is associated with a metamorphic assemblage of chlorite, quartz, calcite, sericite, biotite, muscovite, and K-feldspar (Figure 10b). The chlorite flakes all run parallel to schistosity and show some degree of bending and distortion around quartz and feldspar grains. The mode of occurrence of chlorite with hydrothermal gangue and ore minerals suggest their coprecipitation to relibly estimate the temperature of precipitation.

EPMA mineral chemistry analysis was carried out on a total 5 chlorite samples (4 core samples and 1 surface sample). Four samples are from hydrothermal chlorites in quartz-carbonate veins and one sample from chlorites in micaschist. The hydrothermal chlorites have SiO_2 contents ranging from 27.35 to 34.91 wt%, Al_2O_3 from 17.39 to

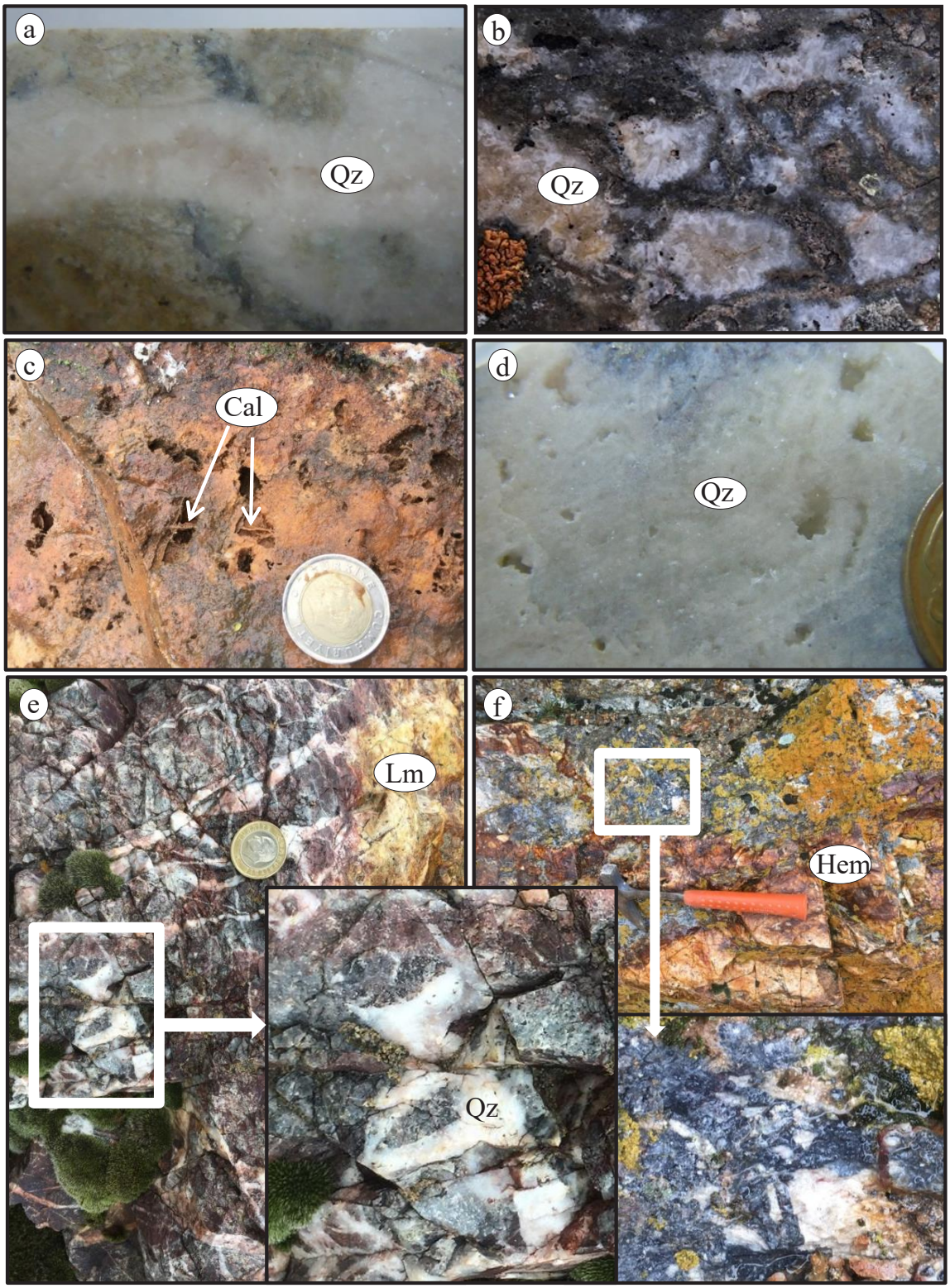

Figure 6. Various textures recognized in quartz-carbonate veins; a) symmetrical comb texture of quartz, b) asymmetrical comb texture by overgrowth of euhedral quartz crystals within the spaces, c and d) various shaped voids partly filled by secondarily grown calcites in quartz-carbonate veins, e) breccia-fill structures (note to a cockade texture in the inlet), f) a chaotic breccia composed of polymictic clasts of preexisting vein infill cemented by a siliceous and hematitic cement (Qz: Quartz, Cal: Calcite, Hem: Hematite, Lm: Limonite).

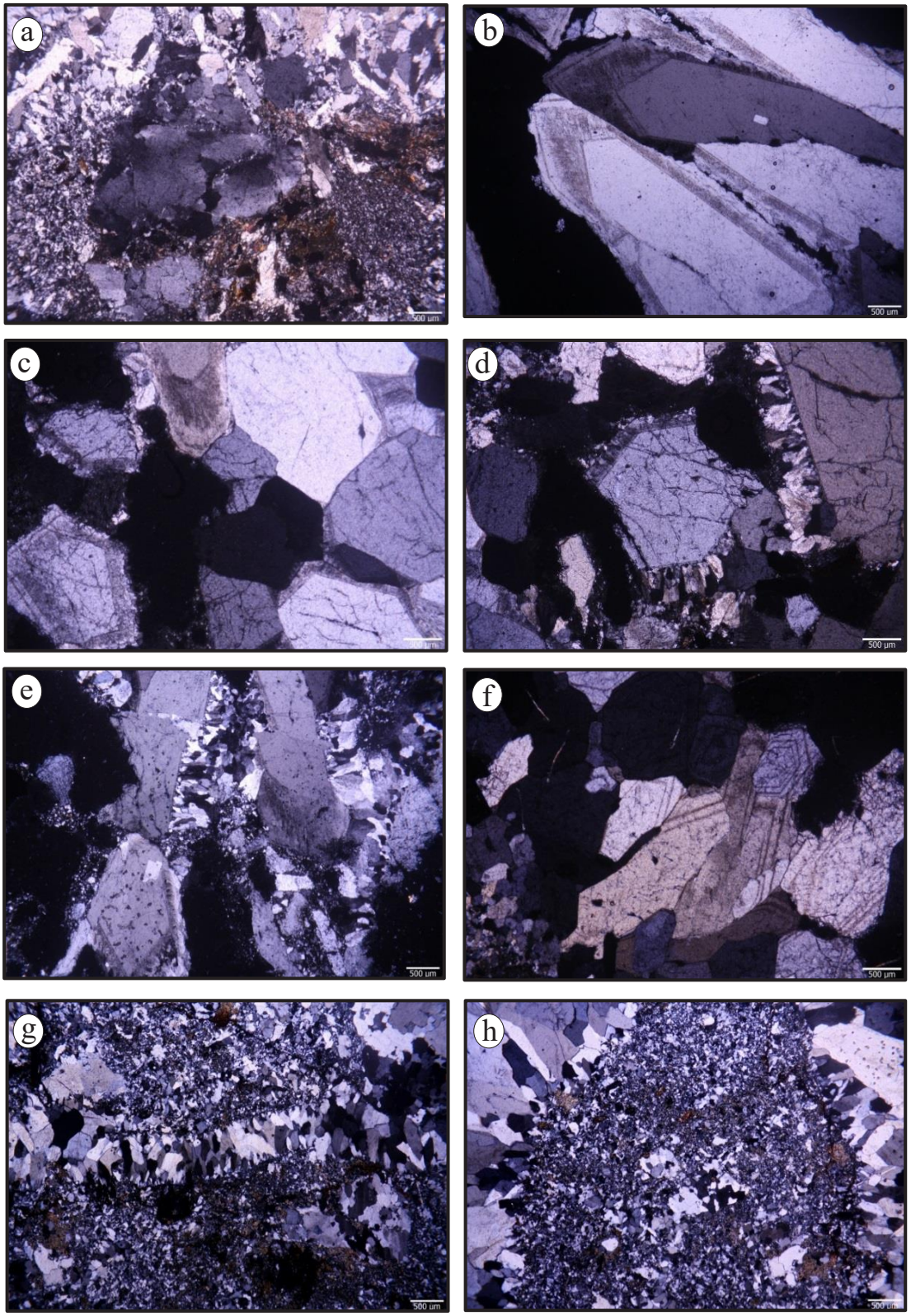

Figure 7. a) Flamboyant texture of euhedral quartz crystals, b, c) feathery texture of euhedral quartz crystals, d and e) plumose texture quartz, f) zoning of euhedral quartz crystals, g) coarse quartz intergrowths along the fillings between small quartz crystals, h) coarse quartz overgrowths around the small quartz crystals.

	Hypogene	Supergene
Pyrite	———	
Chalcopyrite	———	
Gold	———	
Bornite	———	
Tennantite	———	
Quartz	———	
Dolomite	———	
Calcite	———	
Sericite	———	
Chlorite	———	
Rutile	———	
Covellite		———
Malachite		———
Hematite		———
Limonite		———

Figure 8. Paragenetic scheme for the Zarani mineralization.

24.58 wt%, FeO from 14.09 to 21.38 wt%, and MgO from 12.23 to 23.05 wt%. They also have a range of Al^{IV} from 1.25 to 2.23 apfu (based on 28 oxygen) and X_{Fe} from 0.26 to 0.43 apfu. On the contrary, the metamorphic chlorites have less SiO_2 and MgO contents ranging from 25.69 to 29.07 wt% and from 11.86 to 15.67 wt%, respectively and higher FeO contents from 21.49 to 26.24 wt%. The metamorphic chlorites have a range of Al^{IV} from 2.14 to 2.47 apfu and X_{Fe} from 0.44 to 0.55. The hydrothermal chlorites are also enriched with K_2O with respect to the metamorphic chlorites (Table 3). Relatively low Fe contents of the hydrothermal chlorites may be due to the fact that much of the Fe in solution was preferentially incorporated into pyrites, which is the dominant opaque mineral phase in the veins.

In the X_{Fe} vs Al^{IV} diagram, the hydrothermal chlorites are distinctly separated from that of the metamorphic ones with the lower X_{Fe} compositions (Figure 11a). In addition, the metamorphic chlorites display a significant negative correlation (r^2 = –0.86) with Si (apfu) (Figure 11b), whereas those of the hydrothermal chlorites show no or very weak positive correlation (r^2 = 0.33) (Figure 11c).

Hydrothermal chlorites, except one, fall into the field of iron-rich clinochlore whereas metamorphic chlorites are mostly plotted in the Mg-rich chamosite field (Figure 12) (Yavuz et al., 2015).

Although there are several empirical methods to compute the temperature of the formation of chlorites, using those of Cathelineau (1988), Jowett (1991), and

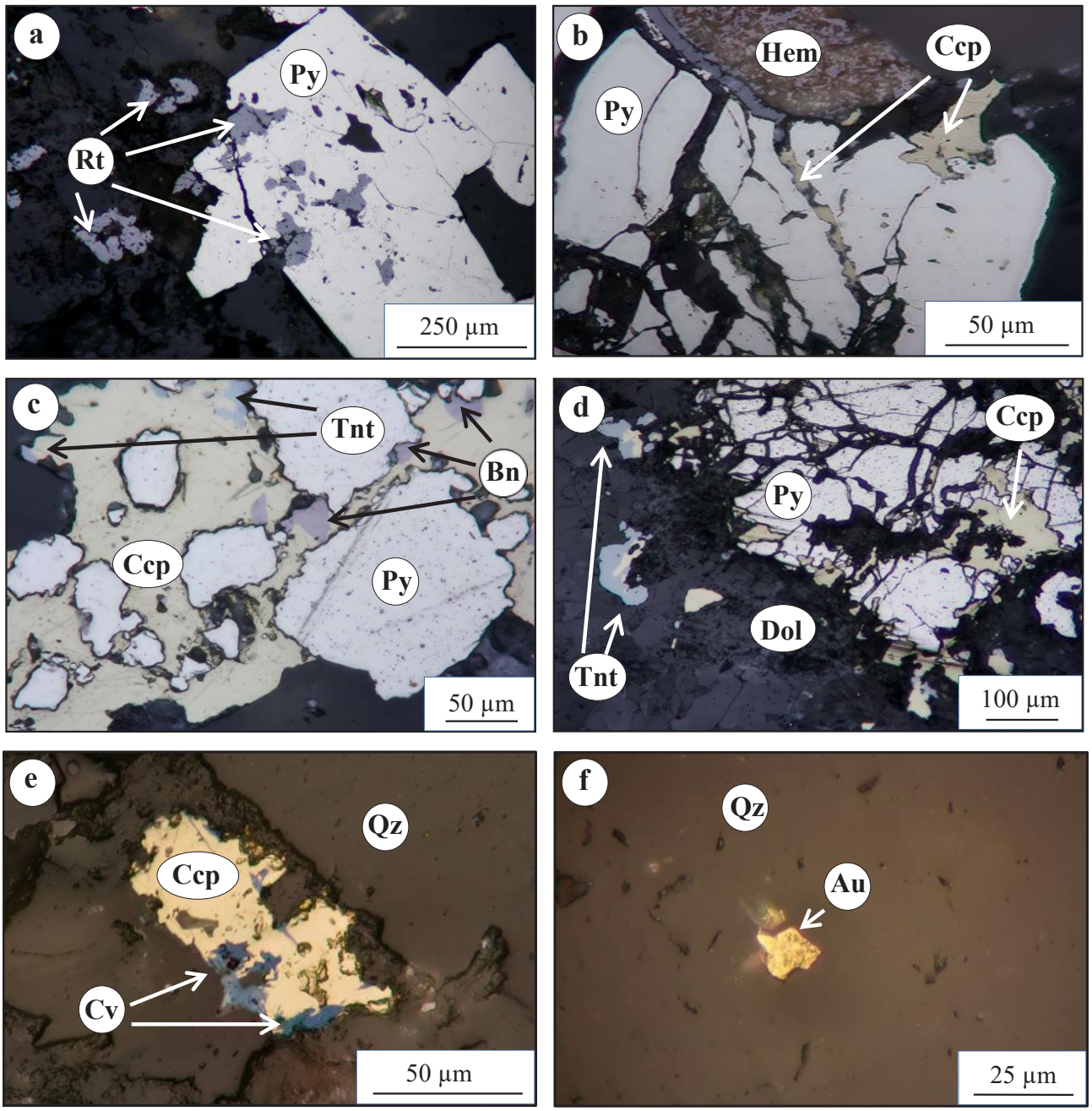

Figure 9. Textural relations between minerals occurring in the Zarani mineralization; a) subeuhedral pyrites with cataclastic texture replaced by rutile, b) pyrite replaced by chalcopyrite and a widely decomposed hematite along the fracture zones, c) subeuhedral pyrite surrounded by chalcopyrite which is replaced by bornite and tennantite, d) anhedral pyrite replaced by chalcopyrite which is also replaced by tennantite, e) anhedral chalcopyrite replaced by covellite, f) gold crystal within the quartz gangue (Py: Pyrite, Rt: Rutile, Ccp: Chalcopyrite, Bn: Bornite, Tnt: Tennantite, Hem: Hematite, Cv: Covellite, Au: Native gold, Qz: Quartz, Dol: Dolomite).

Kranidiotis, and McLean (1987). The temperatures of hydrothermal chlorites are calculated by the formulas of Cathelineau (1988), Jowett (1991) show similar results (ranging from 140 °C to 297 °C) but differ from that (ranging from 178 °C to 280 °C) of Kranidiotis and McLean (1987) (Table 3).

The formation temperatures of the metamorphic chlorites calculated by three of the methods yield similar ranges from 277 to 342 °C (Figure 13).

3.5. Fluid inclusion studies

Fluid inclusion studies are important for understanding physicochemical conditions of ore formation. Description

Table 1. EPMA analyses (wt. %) of pyrites from the Zarani quartz-carbonate veins.

As	S	Sb	Cd	Te	Pb	Ag	Au	Fe	Cu	Zn	Hg	Total
0.000	35.009	0.000	0.000	0.011	0.142	0.016	0.053	29.775	34.735	0.000	0.003	99.7
0.009	54.857	0.000	0.000	0.000	0.122	0.003	0.020	43.622	0.000	0.006	0.000	98.6
0.001	54.559	0.000	0.000	0.019	0.128	0.013	0.065	43.532	0.001	0.000	0.053	98.4
0.000	53.510	0.000	0.010	0.000	0.053	0.000	0.039	46.992	0.011	0.000	0.000	100.6
0.027	53.984	0.000	0.027	0.000	0.024	0.000	0.090	46.980	0.010	0.015	0.090	101.2
0.003	53.571	0.000	0.000	0.000	0.125	0.000	0.128	46.585	0.000	0.005	0.006	100.4
0.000	53.760	0.000	0.030	0.016	0.130	0.004	0.008	46.362	0.000	0.008	0.059	100.4
0.000	53.641	0.013	0.000	0.000	0.143	0.000	0.176	46.577	0.000	0.024	0.000	100.6
0.064	53.362	0.000	0.003	0.007	0.090	0.000	0.075	46.773	0.000	0.000	0.000	100.4
0.043	53.130	0.000	0.014	0.000	0.128	0.039	0.100	46.537	0.000	0.000	0.008	100.0
0.000	34.941	0.013	0.000	0.028	0.037	0.000	0.105	29.804	32.963	0.000	0.022	97.9
0.036	34.689	0.000	0.000	0.021	0.084	0.000	0.089	29.646	32.869	0.000	0.000	97.4
0.000	53.822	0.031	0.000	0.000	0.131	0.002	0.057	46.942	0.000	0.013	0.001	101.0
0.000	53.702	0.000	0.000	0.000	0.153	0.000	0.039	46.775	0.026	0.008	0.000	100.7
0.019	53.547	0.000	0.000	0.023	0.050	0.022	0.121	46.761	0.000	0.000	0.000	100.5
0.000	53.540	0.014	0.020	0.000	0.159	0.000	0.011	46.713	0.009	0.000	0.000	100.5
0.011	53.722	0.000	0.000	0.015	0.115	0.016	0.156	46.477	0.000	0.029	0.000	100.5
0.015	53.096	0.000	0.000	0.000	0.179	0.021	0.080	46.552	0.000	0.012	0.000	100.0
0.002	50.427	0.005	0.010	0.000	0.100	0.010	0.098	44.209	0.000	0.000	0.000	94.9
0.000	52.291	0.000	0.000	0.000	0.115	0.002	0.060	46.356	0.015	0.008	0.000	98.8
0.015	53.560	0.000	0.003	0.000	0.111	0.014	0.173	46.665	0.000	0.013	0.015	100.6
0.000	53.350	0.000	0.000	0.000	0.097	0.019	0.052	46.529	0.010	0.000	0.044	100.1
0.000	53.704	0.000	0.000	0.000	0.047	0.000	0.007	46.348	0.000	0.027	0.000	100.1
0.000	35.198	0.000	0.000	0.000	0.101	0.003	0.093	29.259	32.618	0.000	0.021	97.3
0.012	53.254	0.000	0.000	0.018	0.335	0.002	0.003	45.919	0.450	0.000	0.032	100.0
0.000	34.633	0.000	0.007	0.000	0.140	0.016	0.132	30.071	35.423	0.000	0.000	100.4
0.007	34.667	0.000	0.000	0.000	0.110	0.027	0.037	29.884	34.773	0.000	0.018	99.5
0.001	53.577	0.000	0.000	0.000	0.089	0.000	0.037	46.878	0.182	0.019	0.000	100.8
0.024	53.765	0.024	0.016	0.000	0.127	0.000	0.039	47.193	0.209	0.171	0.049	101.6
0.016	34.874	0.000	0.000	0.000	0.089	0.000	0.137	30.112	33.743	0.000	0.000	99.0

and classification of inclusions are very crucial for the assessment of data obtained from fluid inclusion studies. Fluid inclusions have been classified by various workers with respect to trap mechanisms and composition (Roedder, 1984; Shepherd et al., 1985; Samson and Russel, 1987; Kilias et al., 1996; Wilkinson, 2001). Roedder (1984) classified the fluid inclusions genetically as primary, secondary and pseuydosecondary. Shepherd et al. (1985), made a classification on the basis of phases within the inclusions.

Fluid inclusion studies on quartz-carbonate veins of the Zarani ore field were carried out on 10 quartz samples collected from drill holes and exposures. Measurements were carried out only on primary inclusions, which were classified using the genetic classification criteria by Roedder (1984) and Shepherd et al., (1985). Microscopic examinations reveal that fluid inclusions are represented by gas phase (V) and gas and liquid phase (L + V) compositions (Figure 14). The coexistence of inclusions with only gas phase and gas + liquid phase might indicate boiling process.

Inclusions of gas phase occur only as primary inclusions. Two-phase inclusions ocur as both primary and secondary inclusions. Secondary two-phase inclusions are less than 4 μ in size whereas primary two-phase inclusions have lengths between 3 and 10 μ and contain 5%–10% gas phase.

Table 2. The basic statistical parameters of chemical analysis of borehole and surface samples.

	Minimum	Maximum	Mean	Median	Std. Deviation	Precision %	RSD %
SiO_2 (%)	19.57	98.10	68.40	65.07	23.90	0.67	004
Al_2O_3 (%)	0.28	21.43	9.19	11.30	7.03	2.66	0.05
Fe_2O_3 (%)	0.41	18.42	5.18	4.34	3.98	6.66	0.47
MgO (%)	0.01	0.86	2.79	2.47	2.67	6.09	0.42
CaO (%)	0.01	33.65	3.86	2.61	5.22	6.56	0.33
Na_2O (%)	0.01	3.32	0.67	0.06	0.92	0.00	0.39
K_2O (%)	0.01	4.33	1.20	0.89	1.11	5.05	0.66
Cu (mg/kg)	2.00	370	33.25	14.50	48.49	3.20	0.95
Pb (mg/kg)	0.40	283	21.46	5.25	45.46	0.94	3.67
Zn (mg/kg)	1.00	166	49.43	39.00	39.45	4.33	1.13
Sb (mg/kg)	0.01	13.60	0.86	0.20	2.06	17.39	4.40
As (mg/kg)	0.50	154	15.47	7.85	22.55	5.66	0.90
Au (µg/kg)	0.50	9761	209.61	8.10	1035	17.31	0.20
Hg (µg/kg)	0.01	5.70	0.30	0.08	0.74	0.35	11.50

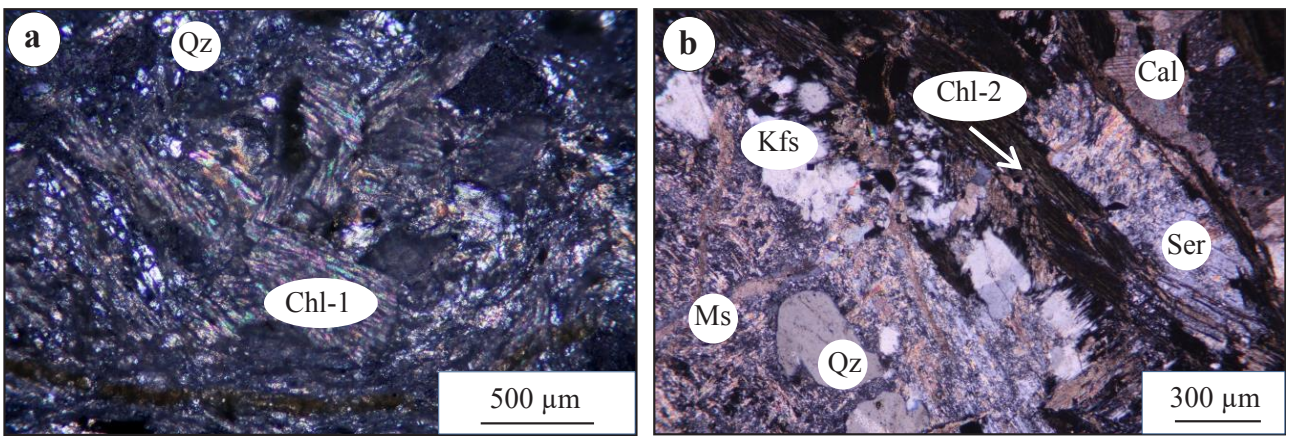

Figure 10. Photomicrographs of chlorite types and associated minerals a) a cluster of equagranular hydrothermal chlorite (Chl-1) in a fine grained quartz matrix, b) metamorphic chlorite (Chl-2) aligned parallel to the foliation planes in the host rock. (Qz: Quartz, Kfs: K-Feldspar, Ser: Sericite, Cal: Calcite, Ms: Muscovite).

The primary inclusions are found in anhedral crystals and show irregular and rarely linear distribution (Figure 14). Inclusions of similar size with only liquid and gas phases are homogenized at nearly the same temperature, which is indicative of boiling (Moncado et al., 2011; Figure 14).

Due to the very small size of fluid inclusions, the first ice-melting temperatures of most inclusions could not be reliably measured. However, some suitable measurements reveal the first ice-melting temperatures in the range of –20 to –18 °C. These temperatures, which are lower than eutectic temperatures suggest a pure H_2O-NaCl system due to the size of very small inclusions and thus starting of first melting cannot be accurately recognized. Data for first ice-melting, salinity and homogenization temperature show normal distributions. Last ice-melting temperatures range from –3.8 to –0.4 °C with an average of –2.64 °C (n = 39) indicating that the salinity values (Figure 15a) are in the range of 0.7 to 6.36 (with an average of 4.32% wt.% NaCl equiv) (Bodnar 1993). Homogenization temperatures of fluid inclusions are between 132 and 226 °C (n = 102, average 165.9, standard deviation 21 °C) (Figure 15b). There is no significant difference between temperatures measured for the surface and the core samples.

According to the BULK program (Bakker, 1999), the densities estimated from homogenization temperatures and salinity values of fluid inclusions (Zhang and Frantz, 1987) are found varying from 0.90 to 0.93 g/cm^3.

Table 3. Some basic chemical composition parameters and properties of two chlorite types and the number of some ions in the unit cell calculated based on 28 Oxygen with temperature of chlorite crystallisation estimated by thermometer of Cathelineau (1988), Jowett (1991), Zang and Fyfe (1995), and Kranidiotis and McLean (1987).

	Hydrothermal chlorite (n = 40)			**Metamorphic chlorite (n = 13)**		
	Min	**Max**	**Average**	**Min**	**Max**	**Average**
SiO_2	27.35	34.91	29.22	25.69	29.07	26.69
TiO_2	0.00	0.07	0.01	0.00	0.11	0. 02
Al_2O_3	17.39	24.58	20.58	20.00	21.81	20.70
FeO	14.09	21.38	17.82	21.49	26.24	24.81
MnO	0.07	0.24	0.15	0.49	0.57	0.53
MgO	12.23	23.05	17.63	11.86	15.67	13.21
CaO	0.04	0.81	0.13	0.00	0.29	0.08
Na_2O	0.00	0.05	0.02	0.00	0.03	0.02
K_2O	0.00	2.86	0.35	0.00	0.07	0.01
Cr_2O_3	0.00	0.04	0.01	0.00	0.04	0.01
H_2O (c)	11.36	12.78	11.80	10.94	12.02	11.60
Cations Based on 28 Oxygen						
Al IV	1.25	2.23	2.01	2.14	2.47	2.31
Si	5.77	6.74	5.98	5.53	5.87	5.69
Fe/(Fe+Mg)	0.26	0.43	0.36	0.44	0.55	0.52
Chlorite Crystallization Temperature						
Cathelineau (1988)	140	297	266	282	336	312
Jowett (1991)	143	297	269	285	342	318
Kranidiotis and McLean (1987)	178	280	263	277	321	303
Properties						
Mineralogy	Quartz-calcite-dolomite-chlorite-sericite			Quartz-K-Feldspar-chlorite-calcite Muscovite-biotite		
Habit	Nonflaky			Flaky		
Mode of occurrences	Equant to rectangular grains and tiny veinlets			Aligned parallel to the schistosity		

3.6. Hydrogen and oxygen systematics

Stable isotopes provide an important information on physical and chemical parameters related to ore formation such as temperature, pressure, depth, chemical composition of fluids, and origin of ore-forming components (Ohmoto, 1986; O'Neil, 1986; Faure, 1986; Hoefs, 1987). During the assessment of isotope data, field observations, relation between ore and gangue minerals and results of fluid inclusion analysis should be taken into account. Results of H and O isotope analyses of quartz minerals from the Zarani ore field are given in Table 4. Oxygen isotope composition of studied quartz-carbonate veins is between 8.6 and 16.1‰.

In order to estimate the $\delta^{18}O_{fluid}$ value, the average homogenization temperature measured on quartz grains (165.9 °C, 439.05 °K) was used. $\delta^{18}O$ composition of fluid/fluids equilibrated with quartz varies from –6.03 to +1.47‰ (O'Neil and Taylor, 1969). If $\delta^{18}O_{water}$ compositions are compared to isotope compositions of various solutions and rocks, the effect of temperature on O isotope composition becomes evident.

4. Analytical methods

4.1. Whole rock geochemistry

Following the petrographic determinations of core and outcrop samples, their major oxides, trace elements analyses were made. Rock samples were crushed with jaw crusher and then grinded to 200-mesh size with tungsten carbide ring crusher at the Geology Department of the Karadeniz Technical University (Turkey). The analyses were carried out at Bureau Veritas Laboratories (Canada, LF-202 analyses package). A powdered sample of 0.2 g was

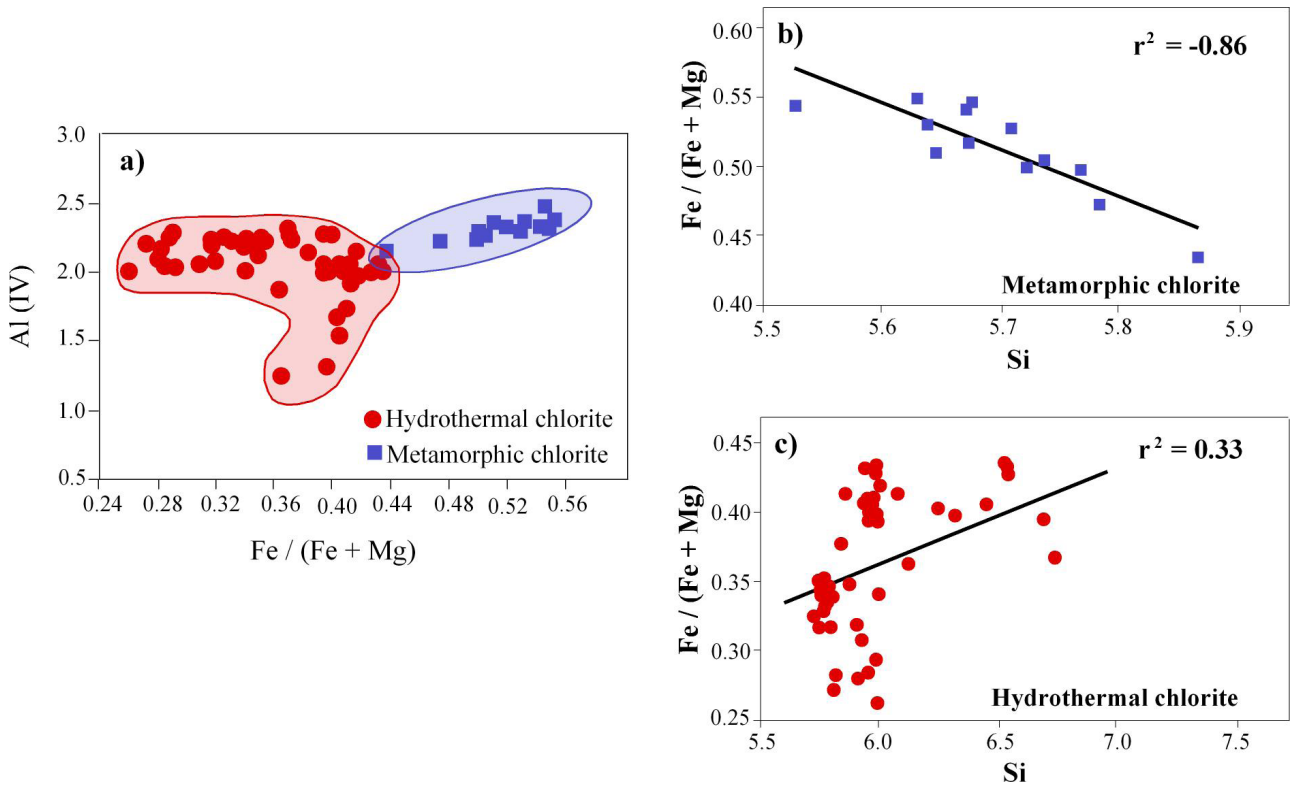

Figure 11. a) Compositonal diagram (X_{Fe} vs. Al(IV)), b) and c) correlation diagram of Si vs. Fe/Fe + Mg for metamorphic and hydrothermal chlorites.

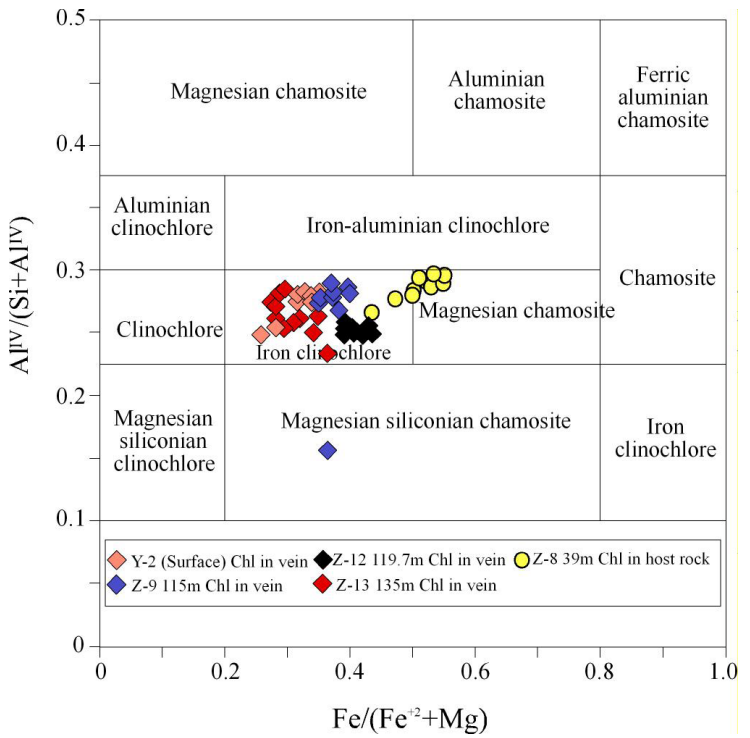

Figure 12. Classification of hydrothermal and metamorphic chlorites (Yavuz et al., 2015).

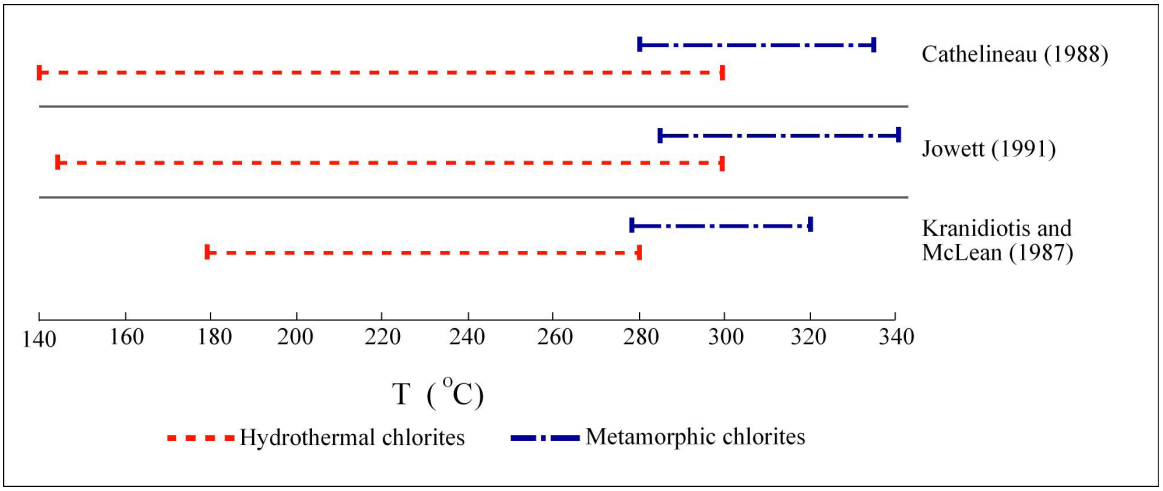

Figure 13. Illustration of temperature ranges of hydrothermal and metamorphic chlorites by thermometers of Kranidiotis and McLean (1987), Cathelineau (1988), Jowett (1991).

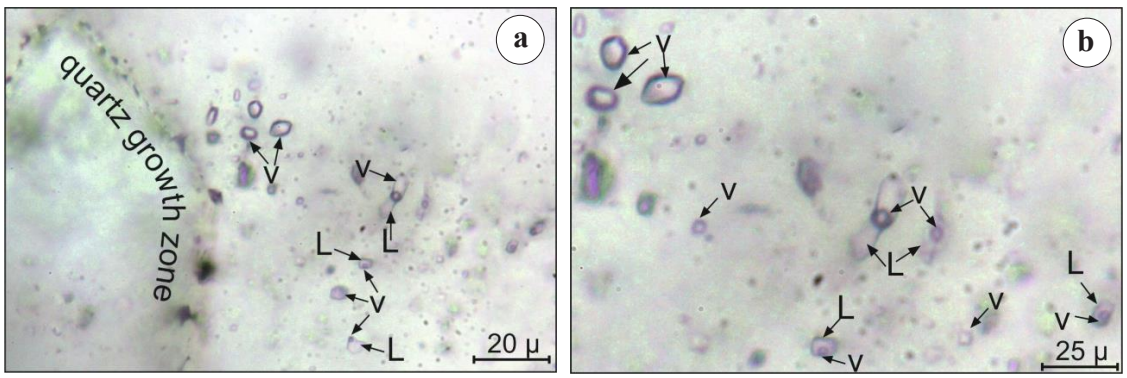

Figure 14. Fluid inclusions images of a quartz sample from the Zarani ore field a) Gas and liquid inclusions over the edge of a euhedral quartz crystal and the area around, b) Enlarged view of fluid inclusions in the juxtaposed area to the euhedral quartz crystal.

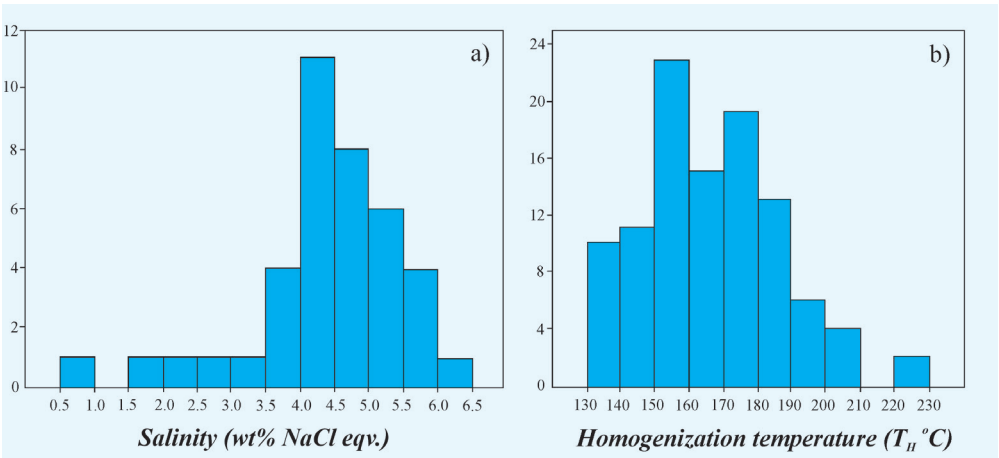

Figure 15. a) Salinities estimated from last melting temperatures, and b) homogenization temperatures (T_H) measured on primary fluid inclusions in quartz.

weighed in a graphite crucible and mixed with 1.5 g $LiBO_2$ flux. Then the mixture was heated at 1050 °C for about 15 min. The melt was dissolved in 100 5% HNO_3 and major oxides were measured with inductively coupled plasma atomic emission spectroscopy (ICP-ES). Rare earth element contents were analyzed with inductively coupled plasma mass spectrometry (ICP-MS) following the dissolution of 0.25 g powdered sample in four different acids. Loss on ignition was estimated from the weight difference after burning the sample at 1000 °C.

4.2. Stable isotope (oxygen and hydrogen) analyses

Oxygen isotope analyses on quartz and hydrogen isotopes from fluid inclusions in quartz were carried out at Queen's Laboratories (Canada). In hydrogen isotope analyses samples were weighed in silver capsules, degassed for 1 h at 100 °C then crushed and loaded into a zero-blank auto sampler. The hydrogen isotopic composition was measured using a Thermo-Finnigan thermo-combustion elemental analyzer (TC/EA) coupled to a Thermo-Finnigan Delta plus XP Continuous-Flow Isotope-Ratio Mass Spectrometer (CR-IRMS). δ^2H values are reported using delta (δ) notation in permil (‰), relative to Vienna Standard Mean Ocean Water (V-SMOW), with a precision of 3‰.

For oxygen isotope analyses, oxygen was extracted from a 5 mg sample at 550–600 °C according to the conventional BrF_5 procedure of Calyton and Mayeda (1963) and analyzed via dual inlet on a Thermo-Finnigan Delta plus XP Isotope-Ratio Mass Spectrometer (IRMS). $\delta^{18}O$ values are reported using the delta (δ) notation in units of permil (‰) relative to the Vienna Standard Mean Ocean Water (V-SMOW) international standard, with a precision of 0.3‰.

4.3. Fluid inclusion analyses

To study fluid inclusions on quartz samples doubly polished wafers were prepared at the laboratories of the Geology Department of the Karadeniz Technical University. Thin sections were examined under a microscope with lenses of ×40 and ×100 magnification to study their types, petrography, and microthermometric characteristics. The measurements were made with Linkam THMSG-600 model liquid nitrogen freezing-heating stage temperature range of –196 °C to 600 °C. The densities and pressures at homogenization of fluid inclusions were calculated using the program compiled by Steele-MacInnis et al., (2012).

4.4. Microprobe analyses

Samples for microprobe analysis were cut with diamond disc of 0.5–1 cm thickness and then using epoxy resin mounted on 28×48 mm thin section glass. Samples were dried for about 8 h and abraded to a thickness of 50–70 µ with diamond discs of 80, 220, 600, and 1200 mesh and finally polished with diamond discs of 6 and 3 µ. The final polishing was made with 1-µ diamond paste and 0.3 and 0.05 µ Al_2O_3 suspensions to Akasel Daran, Akasel Napal and Metkon Fedo1N polishing cloths. The electron microprobe analysis (EPMA) was carried out at the Institute of Petrology and Structural Geology Charles University in 2018 with a JXA-8530F field-emission gun electron microprobe (FEG-EPMA) device equipped with a 5-channel wavelength-dispersive spectrometer. The operating conditions were 15 kV and 30 nA beam current for spot analyses. Samples for EPMA analysis were coated with carbon using the Cressigton brand device. During the measurements natural and synthetic minerals and elements were used for the calibration standard.

5. Results and discussion

5.1. Mineralization and alteration style of the Zarani gold mineralization

The Zarani (Demirözü) gold mineralization is a fault-controlled ore deposit hosted in N40°–60°E trending quartz-carbonate veins with a total length of 1.5 km in the Carboniferous metamorphic rocks. The quartz-carbonate veins show comb, void-filling, breccia-fill/brecciated, mosaic, flamboyant and feathery textures which are typical of epithermal deposits (Yılmaz et.al, 2010, 2013, Fournier, 1985; Dowling and Morrison, 1990; Dong et al., 1995). Since the ore is deposited as open space-filling within fractures and cracks of the wall rock, it reflects an epigenic character. The mineralization is tectonic-controlled and related to Tertiary (?) granitoid intrusions (Eyuboglu et al., 2011; Eyuboglu et al., 2014; Eyuboglu et al., 2017; Eyuboglu et al., 2018).

Table 4. Oxygen and hydrogen isotope compositions of gangue mineral and equilibrated fluids and $\delta^{18}O$ of water in equilibrium with quartz.

Sample No	Mineral	$\delta^{18}O$(‰)	$\delta^{18}O_{water}$(165.9 °C)	δD(‰)
1	Quartz	8.6	–6.03	–119
2	Quartz	14.1	–0.53	–73
3	Quartz	16.1	1.47	–101
4	Quartz	10.4	–4.23	–66
5	Quartz	12.7	–1.93	–60

In epithermal systems, the textures of quartzs significantly change with increasing depth. Comb texture is observed below the boiling level in a deeper part of the vein, whilst brecciated+cockade+banded textures are dominated just above this in the area including the boiling level (Buchanan, 1981). The massive texture is common in shallow parts. Precious metal deposition is related to the boiling process (Giggengbach and Stewart, 1982; Hedenquist et al., 2000). Most quartz textures (Figure 7) are an indication of boiling or sudden temperature and/or pressure decrease which result in rapid precipitation and supersaturation. Boiling first starts at depth and then progresses to the surface. In these systems, gold is enriched in boiling zones where banded, brecciated, and cockade textures occur (Buchanan, 1981; Bodnar et al., 1985; Brown, 1986; Simmons and Christenson, 1994; Andre-Mayer et al., 2002; Etoh et al., 2002; Moncada et al., 2012).

Gold occurs mainly in quartz and carbonate-dominated matrices. However, some sulphide minerals especially pyrites and arsenian pyrites contain a significant amount of invisible gold in their crystal lattice (Fougerouse et al., 2021; Reich et al., 2005). There is no arsenian pyrite among the ore minerals observed but pyrites from Zarani gold mineralization contain considerable amounts of gold (Table 1) and hence contribute significantly to the gold content in quartz-carbonate veins.

The hydrothermal alteration in the Zarani gold mineralization occurs from quartz-carbonate veins to the outer parts of the alteration zone in the order of silicification, carbonatization, sericitization, chloritization, illitization, and kaolinization. Argillic alteration is a common alteration type recognized around the quartz-carbonate veins that form smectite and kaolinite clay minerals in rocks that suffer H^+ metasomatism by hydrothermal solutions with the temperature of 100–300 °C.

5.2. Characteristics of the ore-forming fluids

The Th of fluid inclusions in quartz ranges from 226 °C to 132 °C (Figure 15). The salinities of fluid inclusions in quartz ranged from 6.36 to 0.70 wt%NaCl equivalent. Using homogenization temperature and salinity diagrams (Wilkinson, 2001), the data for fluid inclusions in quartz indicate that mineralization at Zarani involved boiling of a deeply circulated dilute fluid. After the precipitation of gold, the fluid cooled down due to wall-rock interaction (Figure 16). Observation of the vapor and liquid rich inclusions in the same quartz crystals also supports boiling (Figure 14).

The X_{Fe} values of chlorites are related to the oxygen fugacity of the system (Beaufort et al., 1992). A narrow range of the X_{Fe} values (0.43 to 0.55) of the metamorphic chlorites indicates a minor variation in the redox conditions (Pant et al., 2019), whereas a relatively wider range of X_{Fe} values (0.26 to 0.43) of the hydrothermal chlorites suggests a significant fluctuation in fO_2 conditions in the hydrothermal system at the time of their crystallization. The X_{Fe} values of chlorites less than 0.5 point out oxidizing conditions (Pant et al., 2019) prevailing at the time of crystallization of the chlorites and associated minerals. This in turn affirms that increasing fO_2 of the system is caused most probably by the mixing of gold-bearing fluids with oxidizing fluids.

The densities of fluid inclusions in quartz range from 0.9 to 0.93 g/cm^3, and the pressures at homogenization range from 1 to 25 bar. According to hydrostatic pressure conditions, the Zarani gold mineralization formed at a depth shallower than 280 m, beneath the paleo-groundwater table. This is consistent with the Zarani mineralization being an epithermal gold deposit (Cooke and Simmons, 2000; Hedenquist et al., 2000; Simmons et al., 2005; Zhong et al., 2017).

The temperatures calculated from the hydrothermal chlorite EPMA analyses using empirical formulations of Cathelineau (1988), Jowett (1991), Kranidiotis and McLean (1987) range from 140 to 297 °C and homogenization temperatures obtained from fluid inclusions from 132 to 226 °C. Although temperatures obtained from fluid inclusion data show somewhat less temperatures than those from chlorite data, a large range of temperature overlap exists between them.

It might be of interest at this point to compare some fluid characteristics of the Mastra and Arzular gold mineralizations in the region with those of Zarani gold mineralization.

The average homogenization temperature of quartzs from the first stage of mineralization at Mastra is 270 °C and that from the second stage is found at 230 °C. The average salinities on quartz from the first and second stages are 8.4 wt.% and 6.9 wt.% NaCl equiv, respectively (Aslan, 2011). Similarly, the homogenization temperature and salinity of quartzs from Arzular ore field are 214 °C and 8.5 wt.% NaCl equiv, respectively (Akaryalı and Tüysüz, 2013).

It is evident that the average homogenization temperature (165.9 °C) and salinity (4.32 wt.% NaCl equiv) of quartzs from the Zarani field are lower than those of Mastra and Arzular fields. Temperature and salinity values of Zarani field are similar to those of vein-type deposits that are deposited from meteoric fluids with a magmatic component (Roedder, 1984) and this might indicate that the Zarani gold mineralization was formed in an epithermal system. Densities of ore-forming fluids in epithermal deposits generally do not exceed 0.95 g/cm^3 and are always lower than 0.8 g/cm^3 at high temperatures (Roedder, 1984). Densities of fluids in the Zarani field vary from 0.90 to 0.93 g/cm^3 which are largely consistent with those of epithermal deposits.

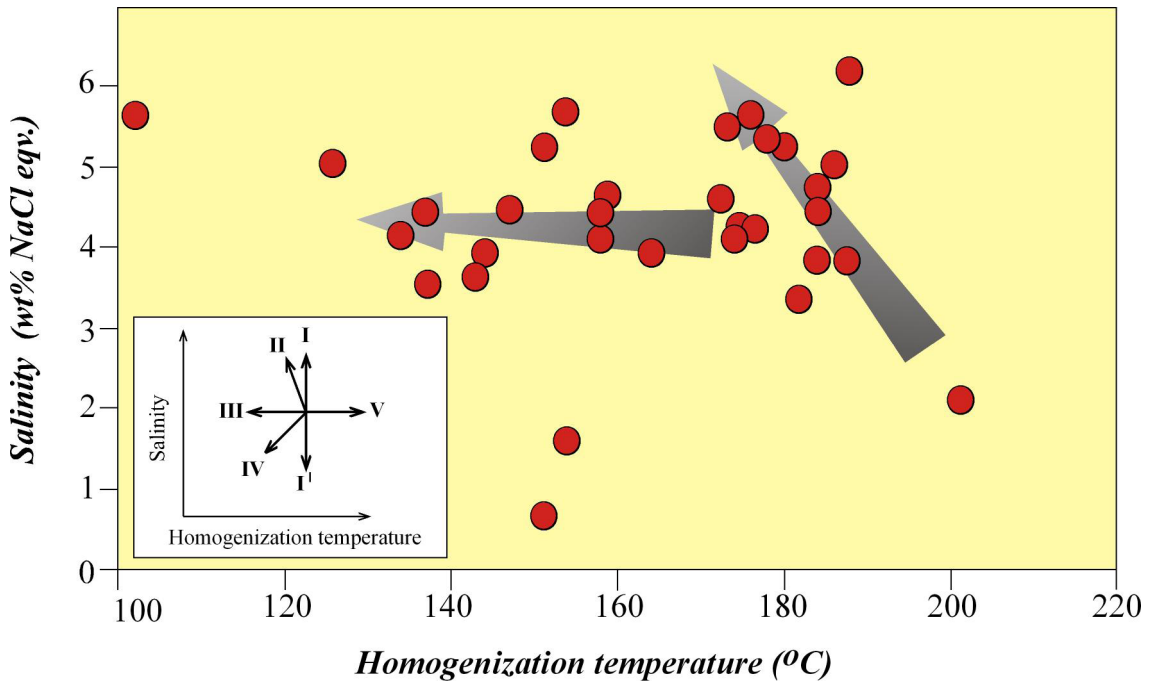

Figure 16. Homogenization temperature and salinity diagrams showing show data for the Zarani gold mineralization (Wilkinson, 2001). The inset figure illustrates temperature–salinity trends or fluid evolution paths as a result of different geological processes (Shepherd et al., 1985). (I) isothermal mixing; (II) boiling; (III) simple cooling; (IV) mixing of fluids with different homogenization temperatures and salinities; (V) leakage.

5.3. Source of ore-forming fluids and gold precipitation

Stable isotope studies can be explicitly used to identify the source, chemical composition, transport, and storage of ore-forming fluids, as well as the temperature of ore formation (e.g., Rye and Ohmoto, 1974; Ohmoto and Rye, 1979; Faure, 2003; Hoefs, 2015). In order to make a comparison between fluids of different origins, H and O isotope compositions of quartz samples from the Zarani gold field are plotted on the diagram proposed by Taylor (1974) and Ohmoto (1986) (Figure 17). H and O isotope values from other gold mineralizations in the nearby regions are also added to the diagram. O and H isotope compositions of quartz samples are –6.03 to +1.47‰ and –60 to –119‰, respectively. Considering the lateral and vertical distributions, the composition of ore-forming fluids is most likely modified by the mixing between magmatic and meteoric waters. The scattered pattern of the data may also indicate local isotopic heterogeneity present during fluid mixing and trapping. In epithermal systems, the hydrothermal solutions are mostly of meteoric origin although magmatic contribution cannot be ruled out (Giggengbach, 1992; Hedenguist and Lowenstern, 1994; Matsuhisa and Aoki, 1994).

Ore-forming fluids in the Mastra and Arzular fields are comprised largely of magmatic waters whereas those in the Zarani field are a mixture of magmatic and meteoric waters. The mixing probably took place before the boiling of magmatic fluids. Boiling as evidenced by quartz texture types (Figure 7), brecciation, and fluid inclusion petrography acts likely the chief process in gold deposition (Figure 16).

5.4. Implications for the Zarani gold deposit type

A combined study of lithology, structural features, fluid inclusions in ore and cogenetic gangue minerals best constrains the ore-forming conditions, particularly for an orogenic epithermal gold deposit. The presence of calcite, dolomite, and sericite in the Zarani gold mineralization indicates the near neutral pH conditions of its ore-forming fluid. The fluid inclusion data for quartz reveal low–medium temperatures and relatively low salinities due to the dilution of magmatic fluids by deeply circulating meteoric waters.

6. Conclusions

Gold mineralization in the Zarani field was formed along N40°–60°E trending quartz-carbonate veins with a thickness of about 10 m and a cumulative length of 1.5 km in the Paleozoic metamorphic units. 60°NW-extending another fracture system in the field does not contain any mineralization. In the Zarani field, gold is accompanied by several metallic minerals such as pyrite, chalcopyrite,

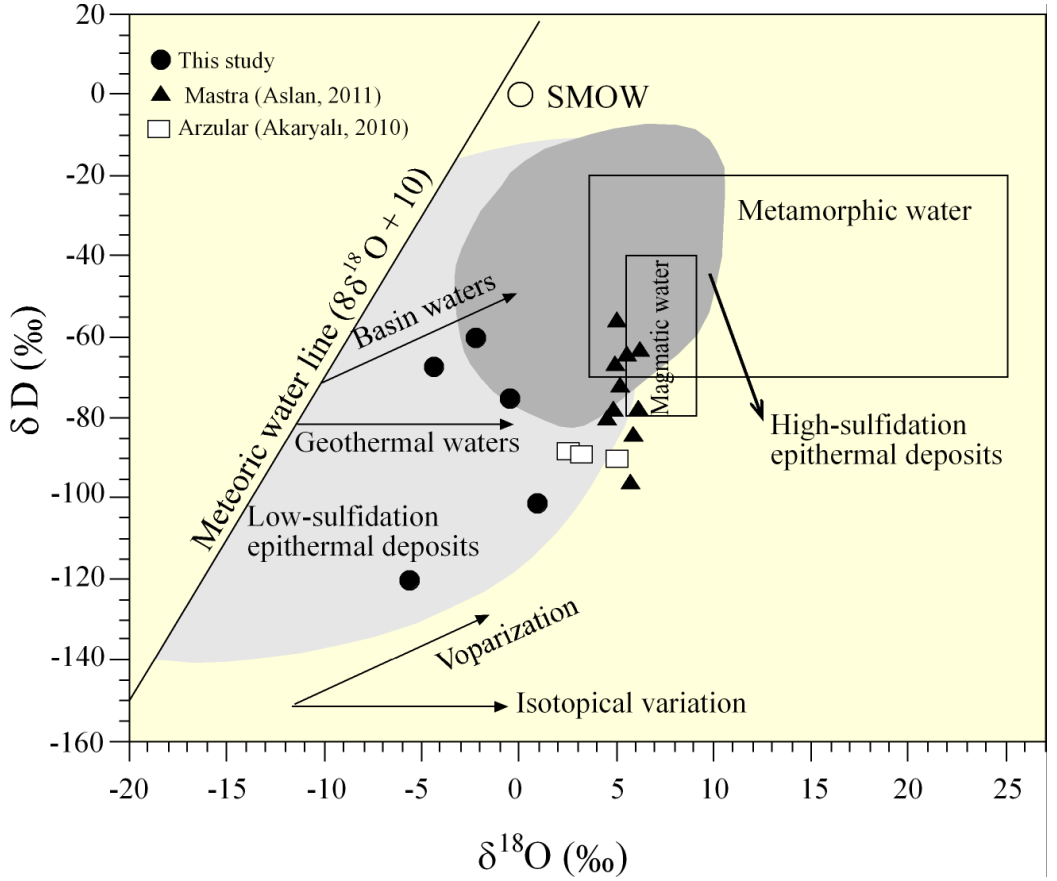

Figure 17. Oxygen and hydrogen isotope compositions of natural solutions. $\delta^{18}O$ and *δD* isotope fractionation graphic for the solutions that precipitated quartz-carbonate veins in the Zarani field (Taylor, 1974; Ohmoto, 1986). The shaded regions are *δD* and $\delta^{18}O$ data for various epithermal deposits compiled by Simmons et al. (2005).

bornite, and tennantite. Quartz, calcite, and dolomite are the major gangue minerals with lesser amounts of sericite and chlorite. Kaolinite and illite are quite abundant around the quartz-carbonate veins. The presence of calcite, dolomite, and sericite in the Zarani gold mineralization indicates the near neutral pH conditions of its ore-forming fluid.

The silica gel hosting gold is deposited during supersaturation that is triggered by faulting and boiling subsequent to rapid pressure and temperature decrease. In the quartz-carbonate veins of the Zarani ore field; massive, comb, space-filling, breccia-fill/brecciated, and zoned growth structures are regarded as the primary growth textures, whilst mosaic, flamboyant and feathery textures are the main recrystallization textures. Many of these textures have resulted from boiling processes that caused gold precipitation. These textures overall indicate depositions from low temperature fluids at shallow levels. The homogenization temperatures and salinities of quartz range from 132 °C to 226 °C and 0.70 to 6.36 wt.% NaCl equiv, respectively. These values are highly compatible with temperatures estimated by the chlorite geothermometer. Although in low abundance, chlorite is one of the main components of the gangue minerals associated with gold. Oxygen (–6.03 to +1.47‰) and hydrogen (–60 to –119‰) isotope compositions of quartz samples vary in a narrow range and lateral and vertical distributions show that the stable isotope composition of ore-forming fluids is modified by mixing between magmatic and meteoric waters. In conclusion, boiling following the mixing of meteoric and magmatic waters enhanced the gold precipitations. The mineralization style and the near-neutral pH conditions of the ore-forming fluid as well as the H–O isotopic data, imply that the Zarani gold mineralization is an orogenic epithermal mineralization that is most likely related to deeply buried Early Cenozoic felsic intrusions.

Acknowledgements
We are very grateful to Dr. Hüseyin Yılmaz and an anonymous reviewer for their valuable contributions which helped to improve the quality of this paper. The

authors are also thankful to Dr. Yener Eyüboğlu and Dr. Osman Bektaş especially for their contributions to the structural geology of this paper. Chemical analyses were conducted at Acme Laboratories in Canada. This study was financially supported by the Scientific Research Project Commission of Karadeniz Technical University (985/5869).

References

Adamia SA, Lordkipanidze MB, Zakariadze GS (1977). Evolution of an active continental margin as exemplified by the Alpine history of the Caucasus. Tectonophysics 40: 183–189.

Adams SE (1920). Microscopic study of vein quartz. Economic Geology 15: 623-644.

Akaryalı E, Tüysüz N (2013). The genesis of the slab window-related Arzular low sulphidation epithermal gold mineralization (eastern Pontides, NE Turkey). Geosci Front 4: 09–421.

Akaryalı E (2016). Geochemical, fluid inclusion and isotopic (O, H and S) constraints on the origin of Pb–Zn ± Au vein-type mineralizations in the Eastern Pontides Orogenic Belt (NE Turkey). Ore Geology Reviews 74: 1-14.

Akaryalı E, Akbulut K (2016). Constraints of C–O–S isotope compositions and the origin of the Ünlüpınar volcanic-hosted epithermal Pb–Zn ± Au deposit, Gümüşhane, NE Turkey. Journal of Asian Earth Sciences 117: 119-134.

Akçay M, Lermi A, Van A (1998). Biogeochemical exploration for massive sulphide deposits in areas of dense vegetation: an orientation survey around the Kankoy Deposit (Trabzon, northeastern Turkey). Journal of Geochemical Exploration 63: 173–187.

Andre´-Mayer AS, Leroy J, Bailly L, Chauvet A, Marcoux E et al. (2002). Boiling and vertical mineralization zoning: a case study from the Apacheta low-sulfidation epithermal gold-silver deposit, southern Peru. Mineralium Deposita 37: 452–464.

Arslan M, Aslan Z (2006). Mineralogy, petrography and whole-rock geochemistry of the Tertiary Granitic Intrusions in the Eastern Pontides, Turkey. Journal of Asian Earth Sciences 27 (2): 177-193.

Aslan N (2011). Geologic, mineralogic and geochemical properties of Mastra (Gümüşhane) Au-Ag deposit (Master Thesis) KTÜ, FBE 190 p.

Aydin F, Saka SO, **Şen** C, Dokuz, Aiglsperger T et al. (2020). Temporal, geochemical and geodynamic evolution of the Late Cretaceous subduction zone volcanism in the eastern Sakarya Zone, NE Turkey: Implications for mantle-crust interaction in an arc setting. Journal of Asian Earth Sciences 192: 104217.

Bakker RJ (1999). Optimal Interpretation of microthermometrical data from fluid inclusions: thermodynamic modelling and computer programming, Habilitation, Ruprecht-Karls-Universität Heidelberg, Germany 54 pp.

Bektaş O (1986) Paleostress trajectories and polyphase rifting in arc-back arc of eastern Pontides. MTA Bulletin 103/104:1-15.

Bektaş O (1987). Volcanic belts as markers of the Mesozoic-Cenozoic active margin of Eurasia: discussion. Tectonophysics 141: 345–347.

Bektaş O, Yılmaz C, Taşlı K, Akdağ K, Özgür S (1995). Cretaceous rifting of the eastern Pontide carbonate platform (NE Turkey): the formation of carbonate breccias andturbidites as evidence of a drowned platform. Giornale di Geologia 57: 233–244.

Bektaş O, Şen C, Atıcı Y, Köprübaşı N (1999). Migration of the Upper Cretaceous subduction-related volcanism toward the back-arc basin of the eastern Pontide magmatic arc (NE Turkey). Geological Journal 34: 95–106.

Bektaş O, Çapkınoğlu Ş, Akdağ K (2001). Successive extensional tectonic regimes during the Mesozoic as evidenced by Neptunian dikes in the Pontide magmatic arc, northeast Turkey. International Geology Review 43: 40–850.

Bodnar RJ, Reynolds TJ, Kuehn CA (1985). Fluid inclusion systematics in epithermal systems. In: B.R. Berger and P.M. Bethke (eds) Feldspar and their reactions. NATO ASI Series C 421: 51-102.

Bodnar RJ (1993). Revised equation and table for determining the freezing point depression of H_2O-NaCl solutions. Geochimica et Cosmochimica Acta 57: 683-684.

Brown KL (1986). Gold deposition from geothermal discharges in New Zeland. Economic Geology 81: 979-983.

Buchanan LJ (1981). Precious metal deposits associated with volcanic environments in the southwest. In relation of Tectonics to ore deposits in the southern Cordillera, Dickinson, W.R. and Payne, W.O., eds, Arizona Geological Society 237-262.

Camprubi A, Albinson T (2007). Epithermal deposits in Mexico-Update of current knowledge and an empirical reclassification. Geological Society of America, Special paper 422.

Cathelineau M (1988). Cation site occupancy in chlorites and illites as a function of temperature. Clay Minerals 23: 471-485.

Cooke DR, Simmons SF (2000). Characteristics and genesis of epithermal gold deposits. In: Hagemann, S.G., Brown, P.E. (Eds.), Reviews in Economic Geology, Vol. 13: Gold in 2000. Society of Economic Geologists, Inc. pp. 221–244.

Çiçek M, Oyman T (2016). Origin and evolution of hydrothermal fluids in epithermal Pb–Zn–Cu ± Au ± Ag deposits at Koru and Tesbihdere mining districts, Çanakkale, Biga Peninsula, NW Turkey. Ore Geology Reviews 78: 176–195.

Delibaş O, Moritz R, Ulianov A, Chiaradia M, Saraç C (2016). Cretaceous subduction-related magmatism and associated porphyry-type Cu–Mo prospects in the Eastern Pontides, Turkey: New constraints from geochronology and geochemistry. Lithos 248-251: 119-137.

Demir Y, Uysal, Sadiklar MB, Sipahi F (2008). Mineralogy, mineral chemistry, and fluid inclusion investigation of Köstere hydrothermal vein-type deposit (Gümüşhane, NE-Turkey). Neues Jahrbuch Fur Mineralogie-Abhandlungen 185 (2): 215-232.

Dewey JF, Pitman WC, Ryan WBF, Bonnin J (1973). Plate tectonics and evolution of the Alpine system. Geological Society of America Bulletin 84: 3137–3180.

Dong G, Morrison GW, Jaireth S (1995). Quartz textures in epithermal veins, Queensland-classification, origin and implications. Economic Geology 90: 1841-1856.

Dowling K, Morrison GW (1990). Application of quartz textures to the classification of gold deposits using north Queensland examples. Economic Geology Monograph 6: 342-355.

Etoh J, Izawa E, Taguchi S (2002). A fluid inclusion study on columnar adularia from the Hishikari low-sulphidation epithermal gold deposit, Japan. Resource Geology 52: 73-78.

Eyuboglu Y, Bektaş O, Seren A, Maden N, Jacoby WR et al. (2006). Three axial extensional deformation and formation of the Liassic rift basins in the Eastern Pontides (NE Turkey). Geologica Carpathica 57 (5): 337–346.

Eyuboglu Y, Dilek Y, Bozkurt E, Bektaş O, Rojay B et al. (2010). Structure and geochemistry of an Alaskan-type ultramafic–mafic complex in the eastern Pontides, NE Turkey. Gondwana Research 18: 230-252.

Eyuboglu Y, Santosh M, Chung SL (2011). Petrochemistry and U-Pb ages of adakitic intrusions from the Pulur massif (Eastern Pontides, NE Turkey): Implications for slab roll-back and ridge subduction associated with Cenozoic convergent tectonics in eastern Mediterranean. The Journal of Geology 119: 394-417.

Eyuboglu Y, Santosh M, Dudas FO, Akaryali E, Chung SL et al. (2013a). The nature of transition from adakitic to non-adakitic magmatism in a slab-window setting: A synthesis from the eastern Pontides, NE Turkey. Geoscience Frontiers 4: 353-375.

Eyuboğlu Y, Santosh M, Yi K, Tüysüz N, Korkmaz S et al. (2014). The Eastern Black Sea-type volcanogenic massive sulfide deposits: Geochemistry, zircon U–Pb geochronology and an overview of the geodynamics of ore genesis. Ore Geology Reviews 59: 29-54.

Eyuboglu Y, Dudas FO, Thorkelson D, Zhu DC, Liu Z et al. (2017). Eocene granitoids of northern Turkey: Polybaric magmatism in an evolving arc–slab window system. Gondwana Research 50: 311-345.

Eyuboglu Y, Dudas FO, Santosh M, Gümrük TE, Akbulut K et al. (2018). The final pulse of the Early Cenozoic adakitic activity in the Eastern Pontides Orogenic Belt (NE Turkey): An integrated study on the nature of transition from adakitic to non-adakitic magmatism in a slab window setting. Journal of Asian Earth Sciences 157:141-165.

Eyuboglu Y, Dudas FO, Zhu D, Liu Z, Chatterjee N (2019). Late Cretaceous I- and A-type magmas in eastern Turkey: Magmatic response to double-sided subduction of Paleo- and Neo-Tethyan lithospheres. Lithos 326: 39-70.

Eyuboglu Y, Dudas FO, Zhu DC, Santosh M, Liu Z et al. (2021). Late Cretaceous alkaline magmas of the Eastern Pontides Orogenic Belt (NE Turkey): A review with new geological, geochemical and geochronological data. Gondwana Research 97: 204-238.

Faure G (1986). Principles of isotope geology, second edition. JohnWiley and Sons, p. 598, New York.

Faure K (2003). δD values of fluid inclusion water in quartz and calcite ejecta from active geothermal systems: do values reflect those of original hydrothermal water? Economic Geology 98: 657–660.

Fournier RO (1985). The behavior of silica in hydrothermal solutions. Geolohy and geochemistry of erpithermal systems, B.R. Berger and P.M. Bethke (ed.). Reviews in Econ. Geology 2: 45-51.

Fougerouse D, Reddy SM, Aylmore M, Yang L, Guagliardo P et al. (2021). A new kind of invisible gold in pyrite hosted in deformation-related dislocations, Geology, The Geological Society of America 49: 1225–1229.

Giggengbach WF, Stewart MK (1982). Processes controlling the isotopic composition of steam and water discharges from steam vents and steam-heated pools in geothermal areas, Geotermics 11/2: 71-80.

Giggengbach WF (1992). Isotopic shifts in waters from geothermal and volcanic systems along convergent plate boundaries and their origin. Earth and Planet Science Letters 113: 495-510.

Güner S, Yazıcı EN (2012) Ore geology report of Bayburt Demirözü-Zarani field. MTA report, Ankara 11583, 78 p.

Güven IH (1993). Geological and Metallogenic Map of the Eastern Black Sea Region. 1: 250000 Map. MTA, Trabzon.

Hedenquist JW, Arribas A, Gonzalez-Urien E (2000). Exploration for epithermal gold deposits. Reviews in Economic Geology 13: 245–277.

Henley RW, Hughes GO (2000). Underground fumaroles: "Excess heat" effects in vein formation. Economic Geology 95 (3): 453–466.

Hoefs J (1987). Stable Isotope Geochemistry. 3rd ed. Springer, Berlin-Heidelberg-New York 241 pp.

Hoefs J (2015). Stable Isotope Geochemistry, seventh edition. Springer International Publishing, Switzerland.

Jowett EC (1991). Fitting iron and magnesium into the hydrothermal chlorite geothermometer. GAC/MAC/SEG Joint Annual Meeting, Program with Abstracts, v. 16, p. A62, Toronto

Karslı O, Chen B, Aydın F, Şen C (2007). Geochemical and Sr-Nd-Pb isotopic compositions of the Eocene Dölek and Sarıçiçek Plutons, Eastern Turkey: implications for magma interaction in the genesis of high-K calc-alkaline granitoids in a post-collision extensional setting. Lithos 98: 67-96.

Kavalieris I, Walshe JL, Halley S, Harrold BP (1990). Dome-related gold mineralization in the Pani Volcanic Complex, North Sulawesi, Indonesia: A study of geologic relation, fluid inclusions and chlorite compositions. Economic Geology 85: 1208– 25.

Kaygusuz A, Yüzel C, Arslan M, Temizel İ, Yi K et al. (2020). Eocene I-type magmatism in the Eastern Pontides, NE Turkey: insights into magma genesis and magma-tectonic evolution from whole-rock geochemistry, geochronology and isotope systematics. International Geology Review 62 (11): 1406-1432.

Kilias SP, Kalogeropoulos SI, Madsen JK (1996). Fluid inclusion evidence for the physical conditions of sulphide depositions in the Olympias carbonate hosted Pb-Zn (Au-Ag) sulphide ore deposit, E. Chalkidiki Peninsula, N. Greece. Mineralium Deposita 31: 394-406.

Kranidiotis P, MacLean WH (1987). Systematics of chlorite alteration at the Phelps Dodge massive sulfide deposit, Matagami. Quebec. Economic Geology 82: 1898- 1911.

Lermi A (2003). Geologic, mineralogic, geochemical and genetic studies of Midi (Karamustafa/Gümüşhane) Zn-Pb deposit, NE-Turkey. (PhD Thesis) KTU, FBE 321 pp.

Maden N, Elmas A (2022). Major tectonic features and geodynamic setting of the Black Sea Basin: Evidence from satellite-derived gravity, heat flow, and seismological data. Tectonophysics 824: 229207. https://doi.org/10.1016/j.tecto.2022.229207

Matsuhisa Y, Aoki M (1994). Temperature and oxygen isotope variations during formation of the Hishikari epithermal gold–silver veins, southern Kyushu, Japan. Economic Geology 89: 1608–1613.

Moncada D, Mutchler S, Nieto A, Reynolds TJ, Rimstidt JD et al. (2012). Mineral textures and fluid inclusion petrography of the epithermal Ag–Au deposits at Guanajuato, Mexico: Application to exploration. Journal of Geochemical Exploration 114: 20-35.

Ohmoto H (1986). Stable isotope geochemistry of ore deposits. In: Valley, J.W., Taylor, H.P., O'Neil, J.R. (Eds.), Stable Isotopes in High Temperature Geological Processes. Reviews in Mineralogy Mineralogical Society of America 16: 491–560.

Ohmoto H, Rye RO (1979). Isotope of Sulfur and Carbon. In: Barnes, H.L. (Ed.), Geochemistry of Hydrothermal Ore Deposits, 2nd edition. John Wiley & Sons, Inc. New York, pp. 509–567.

Okay AI, Şahintürk Ö (1997). Geology of the Eastern Pontides. American Association of Petroleum Geologists Memoirs 68: 291-311.

O'Neil JR (1986). Theoretical and experimental aspects of isotopic fractionation, In: Valley, W. and J.R. O'Neil (eds.), Stable isotopes in high temperatures geological processes, Reviews in Mineralogy 16: 1-40.

O'Neil JR, Taylor BE (1969). Oxygen isotope fractionation between muscovite and water. Journal of Geophysical Research 74: 6012–6022.

Pant S, Singh S, Sahoo PR, Kumar A, Baskaran S et al. (2019). Mineral chemistry and geothermometry of chlorites in relation to physico-chemical conditions of uranium mineralization in the central part of the Singhbhum Shear Zone, eastern India. Ore Geology Reviews 112: 102997.

Reich M, Kesler SE, Utsunomiya S, Palenik CS, Chryssoulis SL et al. (2005). Solubility of gold in arsenian pyrite. Geochimica et Cosmochimica Acta 69: 2781–2796.

Revan MK (2020). Review of Late Cretaceous volcanogenic massive sulfide mineralization in the Eastern Pontides, NE Turkey. Turkish Journal of Earth Sciences 29: 1125-1153.

Roedder E (1984). Fluid inclusions: Reviews in Mineralogy, Mineralogical Society of America 12: 644.

Rye RO, Ohmoto H (1974). Sulfur and carbon isotopes and ore genesis: a review. Economic Geology 69: 826–842.

Samson IM, Russel MJ (1987). Genesis of the silver mines zinc-lead-barite deposit Ireland: Fluid inclusion and stable isotope evidence. Economic Geology 82: 371-394.

Sander MV, Black JE (1988). Crystallization and recrystallization of growth-zoned vein quartz crystals from epithermal systems-implications for fluid inclusion studies. Economic Geology 83: 1052-1060.

Saunders JA (1990). Colloidal transport of gold and silica in epithermal precious-metal systems evidence from the Sleeper deposits, Nevada. Economic Geology 18: 757-760.

Shepherd TJ, Rankin AN, Alderton DHM (1985). A Practical Guide to Fluid Inclusion Studies. Black & Son Press, London 238.

Simmons SF, Christenson BW (1994). Origins of calcite in boiling geothermal system. American Journal of Science 294: 361-400.

Simmons SF, White NC, John DA (2005). Geological characteristics of epithermal precious and base metal deposits. In: Hedenquist, J.W., Thompson, J.F.H., Goldfarb, R.J., Richards, J.P. (Eds.), Economic Geology 100th Anniversary Volume. Society of Economic Geologists, Inc. pp. 485–522.

Steele-MacInnis M, Lecumberri-Sanchez P, Bodnar RJ (2012). Hokıeflıncs-H_2O-NaCl: a Microsoft Excel spreadsheet for interpreting microthermometric data from fluid inclusions based on the PVTX properties of H2O–NaCl. Computers Geosciences 49: 334–337.

Şengör AMC, Yılmaz Y (1981). Tethyan evolution of Turkey: a plate tectonic approach. Tectonophysics 75: 181–241.

Taylor HP (1974). The application of oxygen and hydrogen isotope studies to problems of hydrothermal alteration and ore deposition. Economic Geology 69:843–883.

Tüysüz N, Sadıklar MB, Er M, Yılmaz Z (1995). An Epithermal God-Silver Deposit in the Pontide Island Arc Mastra-Gümüşhane, NE-Turkey. Economic Geology 90 (5): 1301–1309.

Tüysüz N, Çubukçu A (1999). Geology and Geochemistry of the Kaletaş, Gümüşhane, Sediment Hosted Gold Occurance in the Eastern Pontide Island Arc, NE-Turkey, Mineral Deposits: Processes to Processing, Proceedings of the 5th Biennial SGA Meeting, London p. 909-912.

Tüysüz N (2000). Geology, lithogeochemistry and genesis of the Murgul massive sulfide deposit, NE Turkey. Chemie der Erde-Geochemistry 60: 231–250.

Tokel S (1972). Stratigraphical and volcanic history of the Gümüshane Region (NE Turkey) (PhD Thesis, University of College, London).

Wilkinson JJ (2001). Fluid inclusions in hydrothermal ore deposits. Lithos 55: 229–272.

Yaylalı-Abanuz G, Tüysüz N (2010). Chemical, mineralogical, and mass-change examinations across a gold bearing vein zone in the Akoluk area, Ordu, NE Turkey. Neues Jahrbuch für Mineralogie-Abhandlungen 187/1: 11–22.

Yaylalı-Abanuz G, Tüysüz N (2011). Statistical evaluation of the geochemical data from Akoluk epithermal gold area (Ulubey–Ordu), NE Turkey, Geochemical Journal 45: 209-219.

Yavuz F, Kumral M, Karakaya N, Karakaya MÇ, Yıldırım DK (2015). A Windows program for chlorite calculation and classification. Computational Geosciences 81: 101–113.

Yılmaz H, Oyman T, Sonmez FN, Arehart GB, Billor Z (2010). Intermediate sulfidation epithermal gold-base metal deposits in Tertiary subaerial volcanic rocks, Sahinli/Tespih Dere (Lapseki/Western Turkey), Ore Geology Reviews 37: 236–258.

Yılmaz H, Sonmez FN, Akay E, Şener AK, Tezel S (2013). Low-sulfidation epithermal Au-Ag mineralization in the Sındırgı District, Balıkesir Province, Turkey, Turkish Journal of Earth Science 22: 485-522.

Yilmaz TI, Duschl F, Genova DD (2016). Feathery and network-like filamentous textures as indicators for the re-crystallization of quartz from a metastable silica precursor at the Rusey Fault Zone, Cornwall, UK. Solid Earth Sciences 7: 1509–1519.

Zhang YG, Frantz JD (1987). Determination of the homogenization temperatures and densities of supercritical fluids in te system NaCl-KCl-$CaCl_2$-H_2O using synthetic fluid inclusion. Chemical Geology 64: 335-350.

Zhong J, Pirajno F, Chen YJ (2017). Epithermal deposits in South China: geology, geochemistry, geochronology and tectonic setting. Gondwana Research 42: 193–219.